ARTICLES
https://doi.org/10.1038/s41587-021-01155-4

nature biotechnology

A humanized mouse model of chronic COVID-19

Esen Sefik[1], Benjamin Israelow[1,2], Haris Mirza[1,3], Jun Zhao[1,3], Rihao Qu[1,3], Eleanna Kaffe[1], Eric Song[1], Stephanie Halene[4], Eric Meffre[1], Yuval Kluger[3], Michel Nussenzweig[5], Craig B. Wilen[1,6], Akiko Iwasaki[1,7] and Richard A. Flavell[1,7] ✉

Coronavirus disease 2019 (COVID-19) is an infectious disease that can present as an uncontrolled, hyperactive immune response, causing severe immunological injury. Existing rodent models do not recapitulate the sustained immunopathology of patients with severe disease. Here we describe a humanized mouse model of COVID-19 that uses adeno-associated virus to deliver human ACE2 to the lungs of humanized MISTRG6 mice. This model recapitulates innate and adaptive human immune responses to severe acute respiratory syndrome coronavirus 2 infection up to 28 days after infection, with key features of chronic COVID-19, including weight loss, persistent viral RNA, lung pathology with fibrosis, a human inflammatory macrophage response, a persistent interferon-stimulated gene signature and T cell lymphopenia. We used this model to study two therapeutics on immunopathology, patient-derived antibodies and steroids and found that the same inflammatory macrophages crucial to containing early infection later drove immunopathology. This model will enable evaluation of COVID-19 disease mechanisms and treatments.

COVID-19, caused by severe acute respiratory syndrome coronavirus 2 (SARS-CoV-2)[1], is a heterogenous disease with few therapeutic options. Although anti-viral immunity mediates viral clearance in mild COVID-19, robust inflammatory cytokines, decreased circulating lymphocytes and dysregulated myeloid and lymphocyte compartments characterize immunopathology in severe COVID-19 (refs. [2–13]). Accurate model systems are essential to evaluate promising discoveries, but most available rodent and non-human primate models do not reveal the immunopathology seen in patients and are not well suited to test therapeutics in the context of severe COVID-19 or post-acute sequelae of COVID-19 (refs. [14–19]).

ACE2 is a SARS-CoV-2 receptor[20–22]. SARS-CoV-2 does not infect standard laboratory mice owing to differences between mouse and human ACE2 (hACE2) that limit viral entry[14,15,20–22]. Mice with transgenic or transient hACE2 expression can be infected with SARS-CoV-2 (refs. [14,16–19]). Although acute viral response, transmission and vaccine efficacy can be tested in these models, they lack severe, chronic disease (Extended Data Fig. 1). We hypothesized that a functional human immune system would model innate and adaptive human immunity during SARS-CoV-2 infection and confer chronicity and pathology seen in patients. Mice with a human immune system (humanized mice), generated via transplantation of human hematopoietic stem and progenitor cells (HSPCs), are invaluable tools to study the human immune system in vivo[23,24]. MISTRG6 (ref. [25]) mice were engineered by a human/mouse homolog gene replacement strategy to provide physiological expression with regard to quantity, location and time of M-CSF (monocytes and tissue macrophage development)[26], GM-CSF/IL3 (lung alveolar macrophages)[27], SIRPα (macrophage tolerance to human cells)[28], ThPO (hematopoiesis and platelets)[29] and IL6 (improved engraftment and antibody responses)[25,30,31] in a Rag2/γ common chain deleted background. When engrafted with human HSPCs, these mice have a comprehensive immune system similar to humans[25,32]. Delivering hACE2 via an adeno-associated virus (AAV) vector to the lungs allows SARS-CoV-2 infection of HSPC-engrafted MISTRG6 mice. Thus, we created a humanized mouse model of COVID-19 that recapitulates the human innate and adaptive immune systems that is amenable to the mechanistic study of COVID-19 and its myriad of complications.

Results

MISTRG6 humanized mice that transiently express hACE2 can be infected with SARS-CoV-2. We delivered AAV-hACE2 (ref. [17]) to the lungs of immune-reconstituted MISTRG6 mice (*MISTRG6-hACE2*) that were engrafted with human HSPCs (Fig. 1a). *MISTRG6-hACE2* mice were then infected with SARS-CoV-2, which yielded similar viral RNA levels and viral titers to wild-type mice[17] but with prolonged high viral titers and RNA for at least 35 days post-infection (dpi) (Fig. 1b,c, and Supplementary Fig. 1a,b). In contrast, MISTRG6 mice lacking AAV-hACE2 expression did not have detectable viral titers, confirming the necessity of hACE2 for infection (Fig. 1c). Of note, *MISTRG6-hACE2* mice that were infected, but not engrafted, with human HSPCs (and thus lack human immune cells) had lower viral titers than infected mice with human immune cells (Fig. 1c). The presence of human immune cells in *MISTRG6-hACE2* mice caused persistent disease with severe, chronic weight loss for at least 35 dpi (Fig. 1d and Supplementary Fig. 1c). *MISTRG6-hACE2* humanized mice also exhibited more severe lung pathology compared to other animal models[17,18,33–35]. This lung pathology followed the three stages described in human patients with COVID-19: exudative, organizing and fibrotic phases[4,36–39]. At 2 dpi, *MISTRG6-hACE2* mice showed prominent collection of proteinaceous debris in the alveolar spaces, a hallmark of the exudative phase (Fig. 1e and Supplementary Fig. 1d). Lungs at 4 dpi transitioned into organizing phase, highlighted by

[1]Department of Immunobiology, Yale University School of Medicine, New Haven, CT, USA. [2]Department of Medicine, Section of Infectious Diseases, Yale University School of Medicine, New Haven, CT, USA. [3]Department of Pathology, Yale University School of Medicine, New Haven, CT, USA. [4]Section of Hematology, Yale Cancer Center and Department of Internal Medicine, Yale University School of Medicine, New Haven, CT, USA. [5]Laboratory of Molecular Immunology, The Rockefeller University, New York, NY, USA. [6]Department of Laboratory Medicine, Yale University School of Medicine, New Haven, CT, USA. [7]Howard Hughes Medical Institute, Yale University School of Medicine, New Haven, CT, USA. ✉e-mail: richard.flavell@yale.edu

infiltration of alveolar spaces by lymphocytes, macrophages and fibroblasts (Fig. 1e and Supplementary Fig. 1d). Between 14 dpi and 28 dpi, expanding infiltration of inter-alveolar spaces (Fig. 1e and Supplementary Fig. 1d–f) and increasing deposition of collagen, highlighted by thickening of collagen bundles in the lung parenchyma (Fig. 1f and Supplementary Fig. 1d–f), further obliterated alveolar architecture. These changes highlighted the transition from the organizing to the fibrotic phase. The architectural remodeling and collagen deposition was more pronounced at 28 dpi and 35 dpi, resulting in replacement of normal alveolar architecture by dilated cystic spaces, separated by thick interstitial tissue bands (Fig. 1e,f and Supplementary Fig. 1d–f). Thus, these data suggest that humanized *MISTRG6-hACE2* mice model chronic disease and recapitulate the severe, persistent lung pathology seen in patients with severe COVID19.

Inflammatory macrophages and monocytes characterize the immune landscape in SARS-CoV-2-infected *MISTRG6-hACE2* mice. We next characterized human and mouse immune cells in SARS-CoV-2-infected and uninfected *MISTRG6-hACE2* mice by flow cytometry to evaluate the cells that drive immunopathology and viral clearance (Supplementary Fig. 2a,b). The degree of humanization was similar in blood between uninfected and infected mice, but SARS-CoV-2 infection substantially increased recruitment of human immune cells to the lower respiratory tract and lung parenchyma, as quantified in whole lung homogenates and bronchioalveolar lavage (BAL) (Fig. 2a,b). The infiltrates present in lungs and BAL at 2–4 dpi consisted of human monocytes, macrophages and T cells (Fig. 2c), again reminiscent of human COVID-19 lung pathology[7]. In our model, human neutrophils are lacking, so, instead, we measured mouse neutrophils, which are the most abundant mouse immune cells in these mice (Supplementary Fig. 2b). In contrast to persistent human immune cell infiltration, mouse immune cell and neutrophil infiltration was transient, peaking at 4 dpi and returning to baseline by 14 dpi (Supplementary Fig. 2b). Variability in neutrophils is in line with human histopathological findings in lungs[40]. However, the cause of such variability and whether this is a result of superimposed bacterial infections are not established[41,42].

The lung monocytes of infected mice comprised all three human monocyte subsets (CD14$^+$ classical, CD14$^+$CD16$^+$ intermediate and CD16$^+$ non-classical; Fig. 2c). By contrast, and in line with healthy human lung monocytes[43], uninfected humanized mouse lungs harbored only classical CD14$^+$ monocytes, which expanded in response to SARS-CoV-2 infection (Fig. 2c). Intermediate and non-classical monocytes infiltrated infected lungs at high frequencies as early as 2 dpi, peaking at 4 dpi. Macrophage numbers increased at 4 dpi and peaked at 14 dpi, remaining high until 28 dpi (Fig. 2c,d and Supplementary Fig. 2c,d). By 2 dpi, the macrophage compartment was enriched for inflammatory and monocyte-derived macrophages, which outnumbered alveolar macrophages, suggesting that macrophages recruited early from the circulation are the long-term contributors of immunopathology (Fig. 2e–g). Plasmacytoid dendritic cells (pDCs), generally known for their contribution to early anti-viral response and main producers of type I interferon alpha (IFNα), were enriched substantially later in infection (14 dpi in Fig. 2h). Infected mice at 14 dpi also showed activated pDCs (Fig. 2i and Supplementary Fig. 2e) marked by CCR7 and CD83 expression[44]. This coincided with chronically sustained interferon response and sustained inflammatory macrophages, as seen in patients with severe COVID-19 (refs. [7,8,45,46]).

Fig. 1 | MISTRG6 humanized mice that transiently express hACE2 can be infected with SARS-CoV-2. a, Schematic of experimental design. MISTRG6 mice were neonatally reconstituted with human CD34$^+$ cells. After confirmation of human immune cell humanization in circulation, reconstituted MISTRG6 mice were injected with AAV-hACE2 (10^{11} genomic copies per milliliter) intratracheally (*MISTRG6-hACE2*). After a 2-week acclimation and recovery period, *MISTRG6-hACE2* mice were infected intranasally with SARS-CoV-2 (10^6 PFU). **b**, Viral RNA (quantification of N gene) in homogenized lung tissue at 2, 4, 7, 14 and 28 dpi in B6 control or reconstituted or unengrafted MISTRG6 mice expressing or lacking human ACE2. Group 1: $n=4$ (2 dpi), 3 (4 dpi), 3 (7 dpi), 3 (14 dpi) and 3 (28 dpi) biologically independent mice examined over two independent experiments. Group 2: $n=4$ (2–28 dpi) biologically independent mice examined over two independent experiments. Group 3: $n=4$ (2 dpi), 4 (4 dpi), 7 (7 dpi), 4 (14 dpi) and 2 (28 dpi) biologically independent mice examined over three independent experiments. Group 4: $n=4$ (2 dpi), 26 (4 dpi), 6 (7 dpi), 8 (14 dpi) and 8 (28 dpi) biologically independent mice examined over at least four independent experiments. Group 5: $n=3$ (2 dpi), 11 (4 dpi), 3 (7 dpi), 3 (14 dpi) and 2 (28 dpi) biologically independent mice examined over at least two independent experiments. Significance in viral RNA was determined by Mann–Whitney, two-tailed test. Individual values for each mouse and means are presented. **c**, Viral titers measured by PFU (using standard Vero E6 cells) in homogenized lung tissue at 2, 4, 7, 14 and 28 dpi in B6 control or reconstituted or unengrafted MISTRG6 mice expressing or lacking human ACE2. Group 1: $n=4$ (2 dpi), 4 (4 dpi), 2 (7 dpi) biologically independent mice examined over two independent experiments. Group 2: $n=4$ (2 dpi), 4 (4 dpi), 2 (7 dpi) biologically independent mice examined over two independent experiments. Group 3: $n=4$ (2 dpi), 6 (4 dpi), 2 (7 dpi), 3 (14 dpi) biologically independent mice examined over three independent experiments. Group 4: $n=4$ (2 dpi), 11 (4 dpi), 6 (7 dpi), 4 (14 dpi) and 4 (28 dpi) biologically independent mice examined over at least four independent experiments. Group 5: $n=3$ (2 dpi), 7 (4 dpi), 4 (7 dpi), 3 (14 dpi) and 2 (28 dpi) biologically independent mice examined over at least two independent experiments. One-sample *t* and Wilcoxon tests were used for comparison of viral titers. Individual values for each mouse and means are presented. **d**, Weight change during the course of infection plotted as percent change compared to original weight measured just before inoculation with SARS-CoV-2. Group A–D $n=7$ and Group E $n=8$ biologically independent mice examined over at least three independent experiments for 28 d. Means with s.d. are presented. Ordinary one-way ANOVA compared to the mean of uninfected reconstituted MISTRG6 mice (Group A) with Dunnett's multiple comparison test was used. Group E $P<0.0001$; Group D $P=0.2889$; Group C $P=0.8926$; Group B $P=0.9974$. Means with s.d. are plotted. Individual values for Group E are presented in Supplementary Fig. 1c. **e**, Representative images of H&E staining (×2 and ×10 magnification) and box and whisker plot (minimum to maximum) of the histopathological scores and percent area affected of infected (2, 4, 7, 14, 28 and 35 dpi) or uninfected lungs. The whiskers go down to the smallest value (minimum) and up to the largest value (maximum). The box extends from the 25th to 75th percentiles. The median is shown as a line in the center of the box. Uninfected, $n=9$; 2 dpi, $n=5$; 4 dpi, $n=14$; 7 dpi, $n=6$; 14 dpi, $n=11$; 28 dpi, $n=10$; and 35 dpi, $n=6$ biologically independent mice examined over at least three independent experiments. Ordinary one-way ANOVA compared to uninfected lungs was used. *P* value was adjusted by Sidak's multiple comparisons test. **f**, Trichrome staining of infected (2, 4, 7, 14, 28 and 35 dpi) or uninfected lungs. Representative images (×40) and box and whisker plot (minimum to maximum) of the histopathological scores are presented. Arrows indicate areas with collagen deposition. The extent of fibrosis was determined by the thickness of collagen bundles. The whiskers go down to the smallest value (minimim) and up to the largest value (maximum). The box extends from the 25th to 75th percentiles. The median is shown as a line in the center of the box. Uninfected, $n=7$; 2 dpi, $n=3$; 4 dpi, $n=4$; 14 dpi, $n=12$; 28 dpi, $n=8$; 35 dpi, $n=4$ biologically independent mice examined over at least three independent experiments. Ordinary one-way ANOVA compared to uninfected lungs was used. *P* value was adjusted by Sidak's multiple comparisons test. Representative images of all time points are presented as part of Supplementary Fig. 1f. NS, not significant.

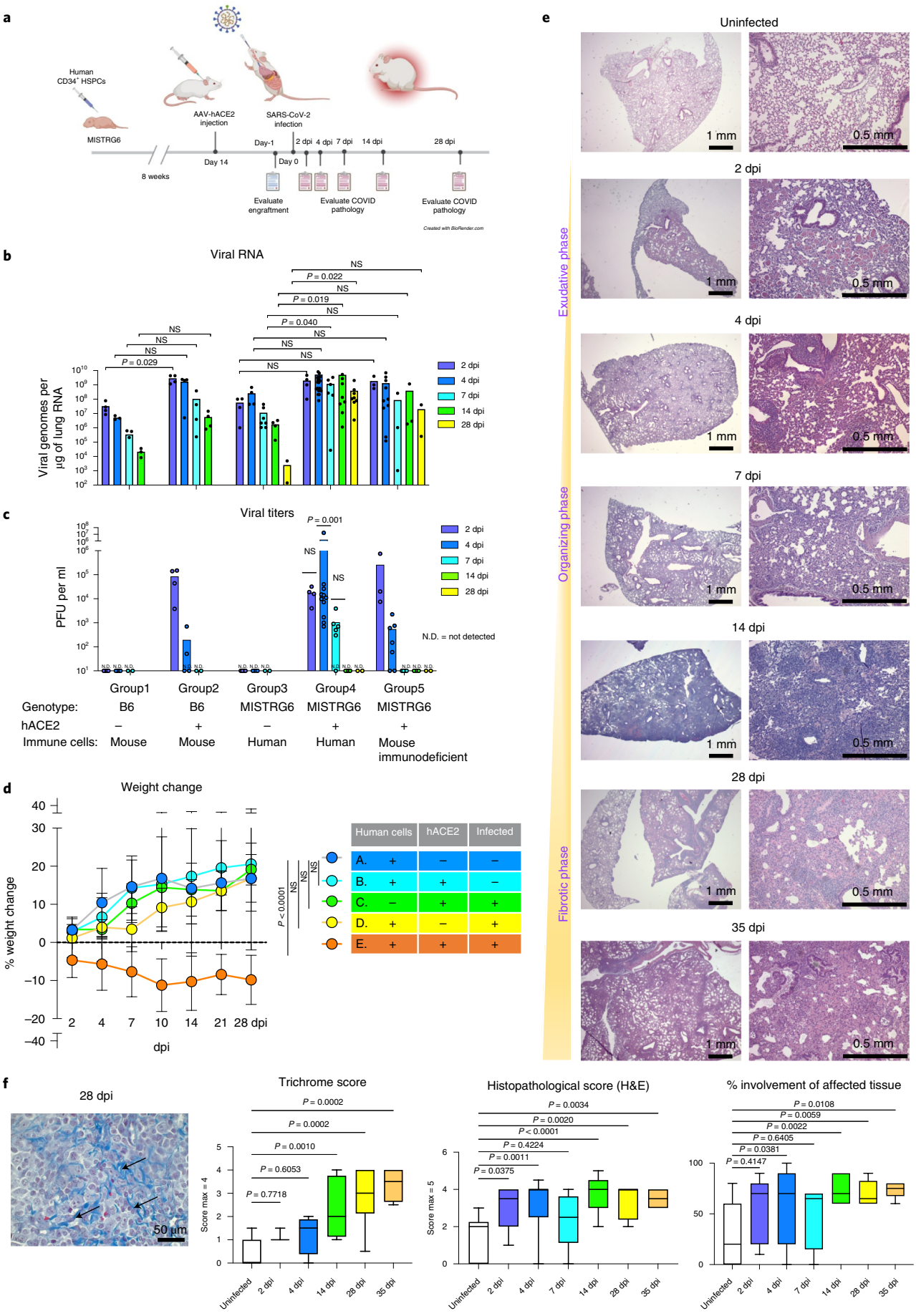
a
Human CD34+ HSPCs
MISTRG6
AAV-hACE2 injection
SARS-CoV-2 infection
8 weeks
Day 14
Day-1
Day 0
2 dpi
4 dpi
7 dpi
14 dpi
28 dpi
Evaluate engraftment
Evaluate COVID pathology
Evaluate COVID pathology
Created with BioRender.com
b
Viral RNA
Viral genomes per µg of lung RNA
2 dpi
4 dpi
7 dpi
14 dpi
28 dpi
c
Viral titers
PFU per ml
N.D. = not detected
Group1 Group2 Group3 Group4 Group5
Genotype: B6 B6 MISTRG6 MISTRG6 MISTRG6
hACE2 – + – + +
Immune cells: Mouse Mouse Human Human Mouse immunodeficient
d
Weight change
% weight change
dpi
Human cells hACE2 Infected
A. + – –
B. + + –
C. – + +
D. + – +
E. + + +
e
Uninfected
2 dpi
4 dpi
7 dpi
14 dpi
28 dpi
35 dpi
1 mm
0.5 mm
Exudative phase
Organizing phase
Fibrotic phase
f
28 dpi
50 µm
Trichrome score
Histopathological score (H&E)
% involvement of affected tissue
Score max = 4
Score max = 5
Uninfected 2 dpi 4 dpi 14 dpi 28 dpi 35 dpi
Uninfected 2 dpi 4 dpi 7 dpi 14 dpi 28 dpi 35 dpi

Adaptive immune responses of patients with COVID-19 are recapitulated in *MISTRG6-hACE2* mice infected with SARS-CoV-2. Human COVID-19 shows profound T cell lymphopenia[10,12,18,47] that is recapitulated in our humanized mice. Infected *MISTRG6-hACE2* humanized mice presented with a profound loss of T cells, especially CD8+ T cells, in blood and spleens (Fig. 3a,b and Extended Data Fig. 2a–c). Moreover, lung T cells of *MISTRG6-hACE2* mice were activated (positive for HLA-DR, CXCR3, ICOS and PD1) and the main producers of IFN-gamma (IFNγ) (Figs. 3c,d and 4b,d), as in patients with COVID-19 (refs. [10–12]). T cell populations comprised both TCRalpha/beta T cells (Tαβ), enriched for CD4+, and TCRgamma/delta T cells (Tγδ) in both uninfected and infected mice (Fig. 3e and Extended Data Fig. 2d). However, during the course of infection, as the circulating T cell numbers decline, the total number of T cells in lungs increased with higher representation of Tγδ cells compared to uninfected mice (Fig. 3e). The early T cell response in infected lungs showed an increase in resident and infiltrating Tγδ cells and bystander-activated memory Tαβ cells as determined by the lung transcriptional profile (Fig. 4b,c and Extended Data Fig. 4h).

As the human cells in these mice develop within a mouse thymus, we sought to determine whether T cells were responsive to virus in the context of major histocompatibility complex developed in our system. To test this, we stained human CD8+ T cells from infected mice that had been engrafted with an HLA-A2-positive source of HSPCs with viral antigen-bearing HLA-A2 tetramers (Extended Data Fig. 2e). Virus-specific CD8+Tαβ cells against membrane glycoprotein (M) and spike (S) peptides were detectable as early as 4 dpi, peaking at 28 dpi (Fig. 3f). To test if these T cells could attenuate infection, we transferred sorted lung T cells and total splenocytes from infected mice to unengrafted *MISTRG6-hACE2* mice before infection with SARS-CoV-2. Viral titers at 4 dpi in mice that received prophylactic lung T cells were clearly lower than mice that did not receive human T cells (Extended Data Fig. 2f). Thus, a functional anti-SARS-CoV-2 T cell response develops in infected *MISTRG6-hACE2* mice.

B cells gradually increased in response to infection, peaking late at 14–28 dpi in BAL and lungs (Fig. 3g and Extended Data Fig. 2g). Although the germinal center B cell response was reported to be suboptimal in reconstituted MISTRG6 mice[30], a high proportion of IgM+ B cells were seen early in infection that were subsequently replaced by IgG+ B cells (14 dpi and 28 dpi) and thus defined the anti-viral B cell response (Fig. 3h,i and Extended Data Fig. 2h). B cells, particularly late in infection, expressed high levels of CD11c (Fig. 3j and Extended Data Fig. 2I), implicating an inflammatory, systemic lupus erythematosus (SLE)-like extrafollicular B cell response[48,49] in humanized COVID-19, reminiscent of the human disease[50]. In contrast to T cell lymphopenia, B cell numbers in the humanized mice were normal or even increased (Fig. 3g and Extended Data Fig. 2j), as in most patients[51]. A robust memory B cell expansion is detected early in human infection, with serum IgM and IgA antibodies detected earlier than IgG[26]. Initial serum IgM and IgA titers in human SARS-CoV-2 infection decline (~28 d) as IgG titers peak (~49 d)[52]. We observed a similar dynamic for IgM+ and IgG+ B cells in humanized lungs, with IgM+ B cells declining over time and IgG+ B cells emerging at 14 dpi and reaching high levels at 28 dpi, at which point serum IgG levels also peak (Fig. 3h,i and Extended Data Fig. 2h,k). Thus, *MISTRG6-hACE2* humanized mice recapitulate T and B cell responses induced by SARS-CoV-2 infection in patients.

SARS-CoV-2 lungs sustain ISGs and display SLE-like features. We evaluated the transcriptional landscape in uninfected

Fig. 2 | Immune landscape in *MISTRG6-hACE2* mice infected with SARS-CoV-2 is characterized by inflammatory macrophages and monocytes. a, Humanization measured by ratio of human CD45+ (human immune cells) cells in total CD45+ cells (mouse and human CD45+ combined) in blood, lungs and BAL of uninfected and infected *MISTRG6-hACE2* mice. Uninfected, n = 8; 2 dpi, $n = 4$; 4 dpi, $n = 7$; 7 dpi, $n = 4$; 14 dpi, $n = 9$; 28 dpi, $n = 4$ biologically independent mice examined over at least three independent experiments. Ordinary one-way ANOVA compared to uninfected lungs was used. *P* value was adjusted with Dunnett's multiple comparison test. Distribution of individual data points is displayed in a violin plot. **b**, Human immune cell numbers in lungs and BAL of uninfected and infected mice at 2, 4, 7, 14 and 28 dpi. Lung: uninfected, n = 11; 2 dpi, $n = 6$; 4 dpi, $n = 7$; 7 dpi, $n = 4$; 14 dpi, $n = 8$; 28 dpi, $n = 5$ over at least three independent experiments. BAL: uninfected, $n = 4$; 2 dpi, $n = 5$; 4 dpi, $n = 6$; 7 dpi, $n = 4$; 14 dpi, $n = 7$; 28 dpi, $n = 4$ over at least three independent experiments. Unpaired, two-tailed *t*-test. *P* values <0.05 are plotted. Individual values for each mouse and means are presented. **c**, Human immune lineages in lungs and BAL of uninfected and infected mice at 2, 4, 7, 14 and 28 dpi within the human CD45+ population. Classical monocytes (CD14+), intermediate monocytes (CD14+CD16+), non-classical monocytes (CD16+CD14−), macrophages (CD68+), NK cells (NKP46+), T cells (CD3+) and B cells (CD19+ and/or CD20+). Statistical significance was deemed by ordinary one-way ANOVA compared to uninfected lungs. *P* values were adjusted with Dunnett's multiple comparison test. *P* values are represented by: NS $P > 0.05$; $^{*}P \leq 0.05$; $^{**}P \leq 0.01$; $^{***}P \leq 0.001$; $^{****}P \leq 0.0001$. Lung: uninfected, $n = 8$; 2 dpi, $n = 4$; 4 dpi, $n = 7$; 7 dpi, $n = 3$; 14 dpi, $n = 9$; 28 dpi, $n = 5$ biologically independent mice examined over at least three independent experiments. BAL: uninfected, $n = 4$; 2 dpi, $n = 4$; 4 dpi, $n = 6$; 7 dpi, $n = 3$; 14 dpi, $n = 6$; 28 dpi, $n = 3$ biologically independent mice examined over at least three independent experiments. *P* values <0.05 are provided, Lung: CD14+CD16+ monocytes, 4 dpi, $P = 0.0003$, and 7 dpi, $P = 0.030$; CD16+ monocytes, 4 dpi, $P < 0.0001$; macrophages, 14 dpi, $P = 0.0114$. BAL: T cells, 2 dpi, $P < 0.0001$; 7 dpi, $P = 0.0003$; 14 dpi, $P = 0.003$; and 28 dpi, $P = 0.001$. Means with s.d. are plotted. **d**, Number of human macrophages in lungs of uninfected and infected mice at 2, 4, 7, 14 and 28 dpi. Unpaired, two-tailed *t*-test. Lung: uninfected, $n = 8$; 2 dpi, $n = 4$; 4 dpi, $n = 7$; 7 dpi, $n = 3$; 14 dpi, $n = 9$; 28 dpi, $n = 6$ biologically independent mice examined over at least three independent experiments. Individual values for each mouse and means are presented. **e**, Frequency and number of human alveolar macrophages marked by CD206hi, CD86+ and CD169+ expression within the hCD45+CD68+ population in the lungs of uninfected and infected mice at 2, 4, 7, 14, 28 dpi. Unpaired, two-tailed *t*-test. Uninfected, $n = 8$; 2 dpi, $n = 4$; 4 dpi, $n = 4$–6; 7 dpi, $n = 3$; 14 dpi, $n = 7$; 28 dpi, $n = 6$ biologically independent mice examined over at least three independent experiments. Individual values for each mouse and means are presented. **f**, Frequency of inflammatory human lung macrophages marked by CD206−/lo and CD86hi macrophages within the hCD45+CD68+ population in the lungs of uninfected and infected mice at 2, 4, 7, 14 and 28 dpi. Unpaired, two-tailed *t*-test. *P* values <0.05 are plotted. Uninfected, $n = 4$; 2 dpi, $n = 4$; 4 dpi, $n = 6$; 7 dpi, $n = 4$; 14 dpi, $n = 7$; 28 dpi, $n = 4$ biologically independent mice examined over three independent experiments. Individual values for each mouse and means are presented. **g**, Frequency of CD16+ human lung macrophages marked by CD16+ cells within the hCD45+CD68+ population in the lungs of uninfected and infected mice at 2, 4, 7, 14 and 28 dpi. Unpaired, two-tailed *t*-test. *P* values <0.05 are plotted. Uninfected, $n = 6$; 2 dpi, $n = 4$; 4 dpi, $n = 8$; 7 dpi, $n = 3$; 14 dpi, $n = 7$; 28 dpi, $n = 6$ biologically independent mice examined over three independent experiments. Individual values for each mouse and means are presented. Unpaired *t*-test, two-tailed. *P* values <0.05 are plotted. **h**, Frequency and number of human pDCs marked by CD123+CD11b−CD11c−/lo cells within hCD45+ population in the lungs of uninfected and infected mice at 2, 4, 7, 14 and 28 dpi. Unpaired *t*-test, two-tailed. Uninfected, $n = 3$; 2 dpi, $n = 2$; 4 dpi, $n = 2$; 7 dpi, $n = 3$; 14 dpi, $n = 7$; 28 dpi, $n = 2$ biologically independent mice examined over at least two independent experiments. Individual values for each mouse and means are presented. **i**, Frequencies of activated, mature (CD83+CCR7+) pDCs in infected lungs at 14 dpi or uninfected lungs. Uninfected, $n = 4$; 14 dpi, $n = 5$ biologically independent mice examined over two independent experiments. Individual values for each mouse and means are presented. Unpaired *t*-test, two-tailed. *P* values <0.05 are plotted. NS, not significant.

and SARS-CoV-2 infected lungs of humanized mice at 2, 4, 7, 14 and 28 dpi. Mapping of transcripts to the human genome or the mouse genome separately identified 285 human genes and 516 mouse genes that were over-represented in infected lungs (Fig. 4a and Supplementary Table 1). This approach served as a proxy for identifying changes in human versus mouse immune cells. Although there was marked heterogeneity in the strength of the response, the anti-viral response was sustained throughout the course of infection, suggesting that early anti-viral responses were either maintained or amplified late in infection (Fig. 4a). Corresponding pathway analysis of these differentially expressed mouse genes (mouse DEGs) identified cellular responses to interferons, cytokine production, ribonuclease activity and neutrophil activation as top biological processes induced during SARS-CoV-2 infection (Supplementary Table 2). Human DEGs were enriched for extracellular matrix assembly, opsonization and complement activation with a focus on immune phenotypes in monocytes, activated T cells and B cells; this further corroborated our findings from flow cytometric analysis (Supplementary Table 2). Similar circuitries of monocytes, macrophages, activated T cells and extrafollicular B cells were described in humans with SARS-CoV-2 pneumonia[50,53].

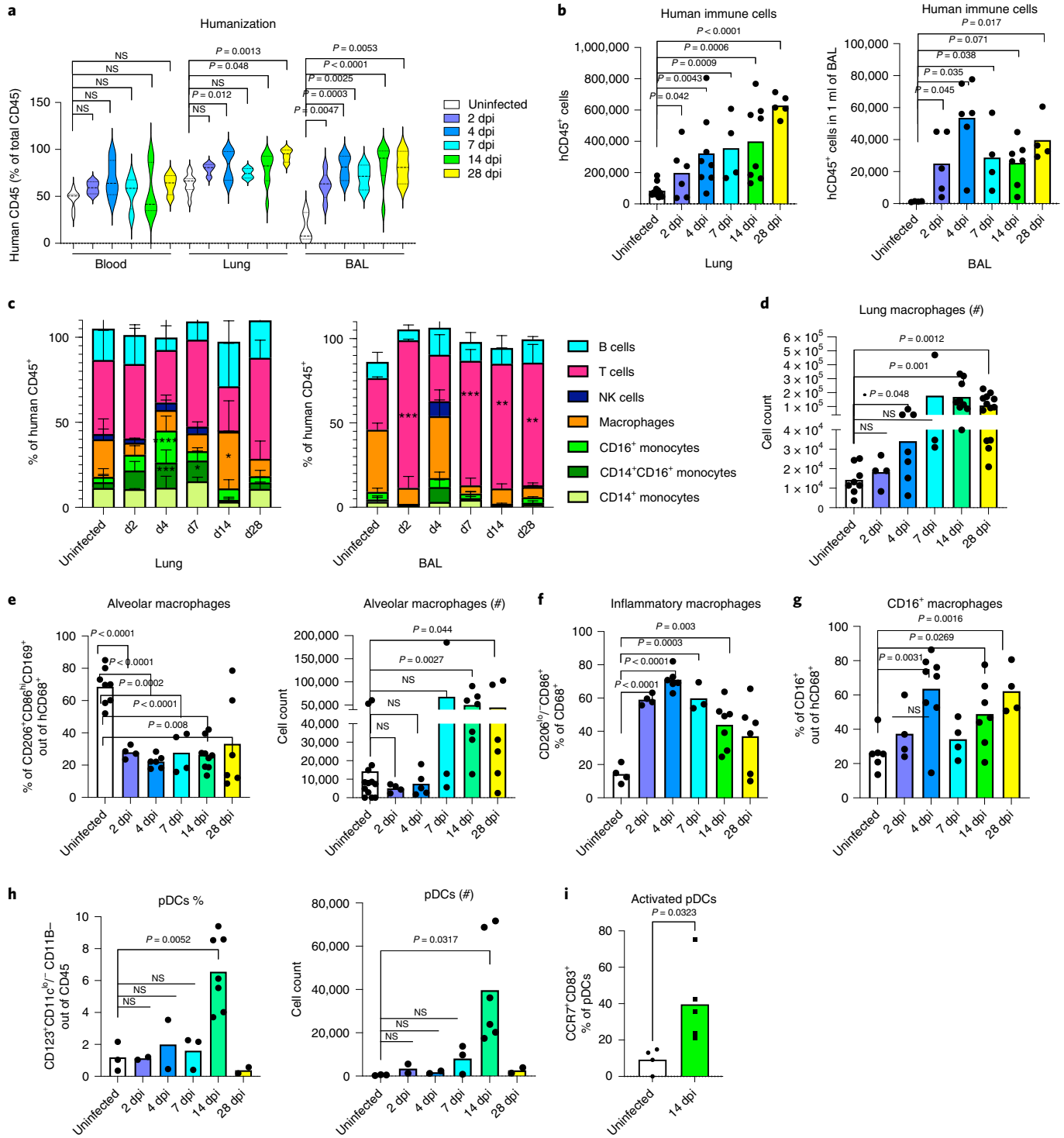

We performed single-cell RNA sequencing to better evaluate the phenotype of human and mouse cells in lungs of infected *MISTRG6-hACE2* mice. Our transcriptome analysis of human cells at the single-cell level also revealed that human macrophages, monocytes and human T cells were abundant at 4 dpi (Fig. 4b,c). Human monocytes infiltrating infected lungs were already differentiating into macrophages at this stage of infection. These infiltrating monocytes and macrophages (clusters 0, 1, 2 and 3) were the main producers of inflammatory cytokines IL1α, IL1β, TNF and IL6, as in patients with severe COVID-19 (refs. [6,9–11,13]) (Fig. 4b,d). As in recent studies characterizing human COVID-19 (ref. [53]), alveolar macrophages in infected *MISTRG6-hACE2* mice were the main producers of T cell chemoattractants, such as *CXCL10* (Fig. 4d). We also monitored mouse immune cells, predominantly enriched for neutrophils (clusters 1 and 2), few mouse monocytes (clusters 5 and 6) and macrophages (cluster 3) at 4 dpi (Extended Data Fig. 3a,b). Mouse neutrophils, which peak at 4 dpi (Supplementary Fig. 1B), were the main producers of mouse inflammatory cytokines and chemokines (*Il1a*, *Il1b*, *TNF*, *Il18* and *Cxcl10*; Extended Data Fig. 3c).

Notably, most of the human and mouse DEGs in lungs were type I or type II interferon-stimulated genes (ISGs) (Fig. 4e and Supplementary Tables 1–3). ISGs were sustained at high levels throughout infection, persisting even as late as 14 dpi and 28 dpi, recapitulating the interferon-dependent phenotypes identified in patients with COVID-19 (Fig. 4a,e and Supplementary Tables 2 and 3)[13,45,46,54]. Despite their fundamental role in many infectious and inflammatory diseases, the direct quantitation of type I interferons has been challenging in health and disease[55]. Despite a significant ISG signature, minimal amounts of type I interferons have been detected in the blood or lungs of patients with severe COVID-19 (refs. [56–59]). This contrasts with those seen in patients infected with highly pathogenic influenza viruses[60]. We first quantified type I interferons by qPCR. Of the many *IFNA* gene transcripts we tested (*IFNA1*, *IFNA2*, *IFNA6*, *IFNA8*, *IFNA14* and *IFNA21*), only *IFNA1* and *IFNA6* mRNA levels were reliably detected and increased upon infection with SARS-CoV-2, peaking at 14 dpi and coincident with pDC numbers in the lung tissue (Fig. 4f). We observed a similar, but not significant, trend for *IFNB* levels (Extended Data Fig. 3d). Next, we quantified IFNα levels by ELISA in infected and uninfected mice. IFNα levels in serum and BAL, although low, mir-

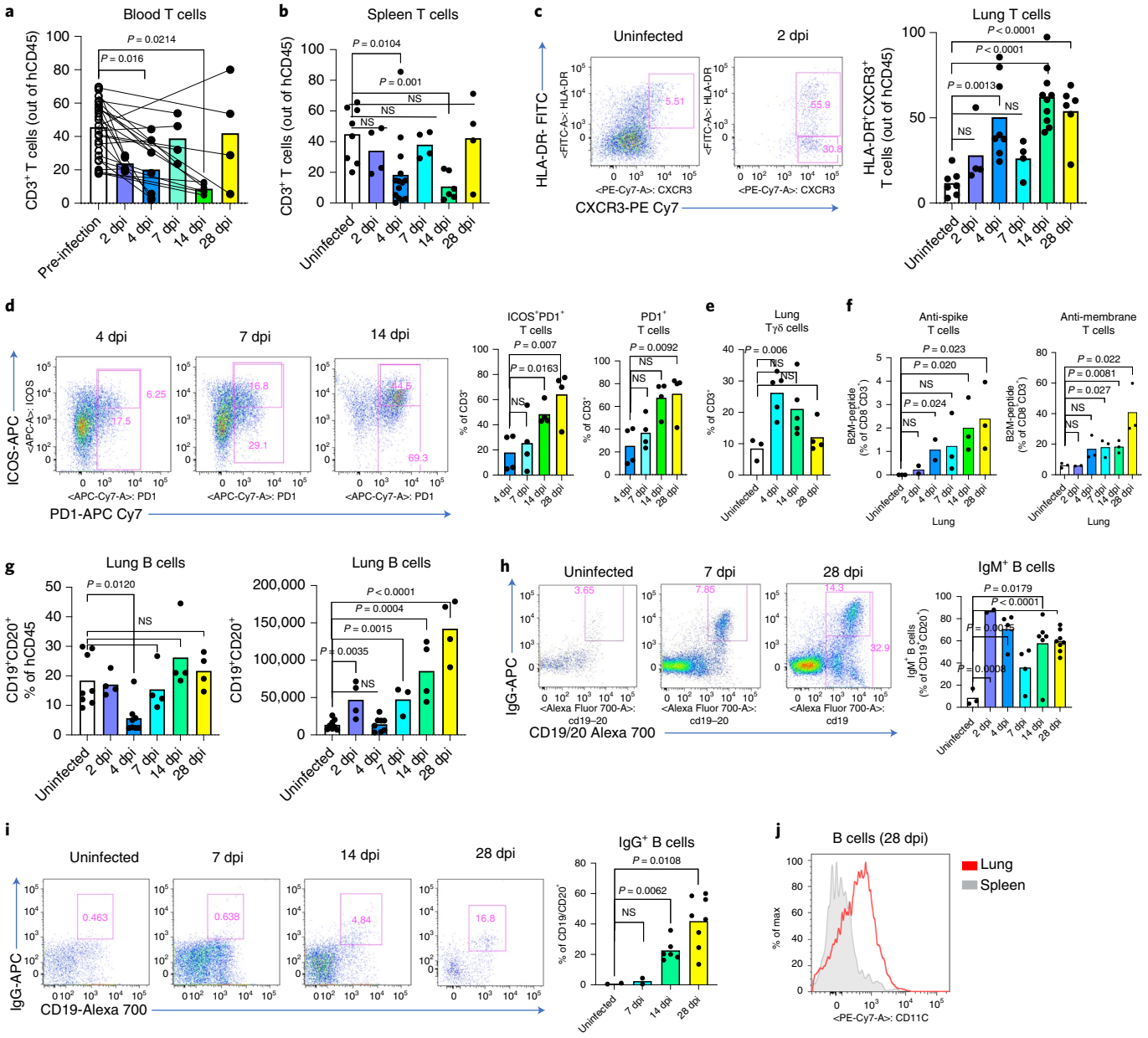

Fig. 3 | Adaptive immune responses in *MISTRG6-hACE2* mice infected with SARS-CoV-2 are characterized by virus-specific activated T cells, IgG⁺ B cells and systemic lymphopenia. a, Frequencies of human CD3⁺ T cells within human CD45⁺ population in the blood before and after infection (2, 4, 7, 14 and 28 dpi). Lines connect pre- and post-infection values for the same mouse. Paired, two-tailed *t*-test. 2 dpi, $n=4$; 4 dpi, $n=7$; 7 dpi, $n=4$; 14 dpi, $n=6$; 28 dpi, $n=4$ biologically independent mice examined over three independent experiments. Individual values for each mouse and means are presented. *P* values <0.05 are plotted. **b**, Frequencies of human CD3⁺ T cells within human CD45⁺ population in the spleens of uninfected and infected mice at 2, 4, 7, 14 and 28 dpi. Uninfected, $n=8$; 2 dpi, $n=4$; 4 dpi, $n=14$; 7 dpi, $n=4$; 14 dpi, $n=6$; 28 dpi, $n=4$ biologically independent mice examined over at least three independent experiments. Unpaired, two-tailed *t*-test. Individual values for each mouse and means are presented. *P* values <0.05 are plotted. **c**, Representative flow cytometry plots of HLA-DR and CXCR3 expression on human lung T cells and frequencies of HLA-DR⁺CXCR3⁺ lung T cells in uninfected and infected mice at 2, 4, 7, 14 and 28 dpi. Uninfected, $n=7$; 2 dpi, $n=4$; 4 dpi, $n=8$; 7 dpi, $n=4$; 14 dpi, $n=9$; 28 dpi, $n=6$ biologically independent mice examined over at least three independent experiments. Unpaired, two-tailed *t*-test. Individual values for each mouse and means are presented. *P* values <0.05 are plotted. **d**, Representative flow cytometry plots of ICOS and PD1 expression on human lung T cells and frequencies of ICOS⁺PD1⁺ or PD1⁺ T cells in uninfected and infected mice (4, 7, 14 and 28 dpi). $n=4$ biologically independent mice examined over at least three independent experiments. Unpaired, two-tailed *t*-test. Individual values for each mouse and means are presented. *P* values <0.05 are plotted. **e**, Frequencies of TCRgamma/delta T cells (Tγδ) among human lung T cells in uninfected and infected mice (4, 14 and 28 dpi). Uninfected, $n=3$; 4 dpi, $n=5$; 14 dpi, $n=5$; 28 dpi, $n=4$ biologically independent mice examined over at least three independent experiments. Unpaired, two-tailed *t*-test. Individual values for each mouse and means are plotted. *P* values <0.05 are plotted. **f**, Frequencies of anti-viral CD8⁺ T cells in uninfected and infected mice at 2, 4, 7, 14 and 28 dpi. Human CD8⁺ T cells from mice that were engrafted with an HLA-A2-positive source of progenitor cells were stained with viral antigen (peptides of M and S viral proteins)-bearing HLA-A2 tetramers. Uninfected, $n=3$; 2 dpi, $n=2$; 4 dpi, $n=3$; 7 dpi, $n=3$; 14 dpi, $n=3$; 28 dpi, $n=3$ biologically independent mice examined over two independent experiments. Unpaired, two-tailed *t*-test. Individual values for each mouse and means are presented. *P* values <0.05 are plotted. **g**, Frequencies and numbers of human B cells within hCD45⁺ population in the lungs of uninfected or infected mice at 2, 4, 7, 14 and 28 dpi. Uninfected, $n=8$; 2 dpi, $n=4$; 4 dpi, $n=8$; 7 dpi, $n=4$; 14 dpi, $n=4$; 28 dpi, $n=4$ biologically independent mice examined over at least two independent experiments. Unpaired, two-tailed *t*-test. Individual values for each mouse and means are presented. *P* values <0.05 are plotted. **h**, Representative flow cytometry plots and frequencies of IgM⁺ B cells in the lungs of uninfected and infected mice at 2, 4, 7, 14 and 28 dpi. Unpaired, two-tailed *t*-test. *P* values <0.05 are plotted. Uninfected, $n=3$; 2 dpi, $n=2$; 4 dpi, $n=4$; 7 dpi, $n=4$; 14 dpi, $n=6$; 28 dpi, $n=8$ biologically independent mice examined over at least two independent experiments. Unpaired, two-tailed *t*-test. Individual values for each mouse and means are presented. *P* values <0.05 are plotted. **i**, Representative flow cytometry plots and frequencies of IgG⁺ B cells in the lungs of uninfected and infected mice at 7, 14 and 28 dpi. $n=2$–8. Unpaired, two-tailed *t*-test. *P* values <0.05 are plotted. Uninfected, $n=2$; 7 dpi, $n=2$; 14 dpi, $n=6$; 28 dpi, $n=8$ biologically independent mice examined over at least two independent experiments. Unpaired, two-tailed *t*-test. Individual values for each mouse and means are presented. *P* values <0.05 are plotted. **j**, Representative plot of CD11c expression on CD19⁺ B cells from spleen and lungs of infected mice at 28 dpi. $n=5$. Representative of $n=6$ for at least three independent experiments. All attempts resulted in similar findings. NS, not significant.

rored transcript levels primarily produced by lung pDCs (Extended Data Fig. 3e,f). Interferons during the recovery phase of influenza infection have been shown to prevent epithelial cell proliferation and differentiation, hence interfering with lung repair[61]. Likewise, our findings suggest that sustained type I interferon signaling might also contribute to persistent lung pathology in COVID-19, as supported by histopathological assessment of 14–28-dpi lungs, when interferon levels are particularly high (Fig. 1e,f and Supplementary Table 3). Human and mouse DEGs were also enriched for type II ISGs (Fig. 4e). Type II interferon, *IFNG*, was mainly produced by T cells (Fig. 4d) as early as 2 dpi and sustained until 28 dpi. (Fig. 4g and Extended Data Fig. 3g). In addition, elevated levels of various pro-inflammatory cytokines and chemokines (*IL6*, *IL8*, *TNF*, *IL1B*, *CXCL10* and *IFNG*) peaked or remained high late in infection, further supporting delayed immune resolution (Fig. 4g). An inflammatory cytokine signature (particularly IL6 (refs. [6,10]) and IL8 (ref. [62])), recapitulated in our model, was closely correlated with COVID-19 severity in patients[6,63]. Elevated serum TNFα levels were

Fig. 4 | SARS-CoV-2 lungs sustain ISGs and display SLE-like features. a, Heat map of differentially regulated human and mouse genes (combined list of genes $\log_2$ fold change >1 in each infected time point versus uninfected lungs; adjusted $P < 0.05$; mean normalized count >5). Transformed normalized counts in lungs of uninfected or infected *MISTRG6-hACE2* mice plotted over the course of infection were clustered using the Spearman correlation. Row minimum and maximum of transformed values, calculated by subtracting row mean and dividing by the s.d. for each gene across all samples, are visualized. For the adjusted *P* values the Bonferroni correction was used. Human genes: uninfected, $n=5$; 2 dpi, $n=4$; 4 dpi, $n=7$; 7 dpi, $n=3$; 14 dpi, $n=2$; 28 dpi, $n=2$ biologically independent mice examined over at least two independent experiments for all time points. Mouse genes: uninfected, $n=5$; 2 dpi, $n=4$; 4 dpi, $n=9$; 7 dpi, $n=3$; 14 dpi, $n=4$; 28 dpi, $n=2$ biologically independent mice examined over at least two independent experiments for all time points. Whole tissue lung samples with less than 1% human reads were excluded from analysis (pre-established criterion). **b**, *t*-SNE plot with clustering results of single-cell RNA sequencing of human immune cells using the 10x Genomics platform from lungs at 4 dpi. Single-cell suspensions from whole infected lung at 4 dpi were processed and sequenced. There were 421 cells identified as human immune cells. **c**, Dot plot of cluster identifying genes for human immune cell clusters described in Fig. 4b. **d**, Cluster distribution and expression profile of human inflammatory cytokines for clusters described in Fig. 4b,c. **e**, Distribution of ISGs within human and mouse DEGs. **f**, Normalized expression of human *IFNA1* and *IFNA6* mRNA measured by qPCR in homogenized lung tissue of uninfected and infected (2, 4, 7, 14 and 28 dpi) mice. Expression was normalized to human HPRT1. Unpaired *t*-test, one-tailed, because the distribution is expected to be one-sided. Uninfected, $n=6$; 4 dpi, $n=4$; 7 dpi, $n=3$; 14 dpi, $n=9$; 28 dpi, $n=3$ biologically independent mice examined over at least three independent experiments. Individual values for each mouse and means are presented. *P* values <0.05 are plotted. **g**, Normalized counts for inflammatory cytokines implicated in patients with COVID-19. Counts were reported separately for human (red) and mouse (blue) cytokine genes, based on whole tissue transcriptome data presented in Fig. 4a. Human genes: uninfected, $n=5$; 2 dpi, $n=4$; 4 dpi, $n=7$; 7dpi, $n=3$; 14 dpi, $n=2$; 28 dpi, $n=2$ biologically independent mice examined over at least two independent experiments for all time points. Mouse genes: uninfected, $n=5$; 2 dpi, $n=4$; 4 dpi, $n=9$; 7 dpi, $n=3$; 14 dpi, $n=4$; 28 dpi, $n=2$ biologically independent mice examined over at least two independent experiments for all time points. **h**, Heat map of genes that are implicated in SLE-like B cells based on GSE10325 (ref. [67]) in infected lungs of MISTRG6 mice at 2, 4, 7, 14 and 28 dpi. Row minimum and maximum of transformed values, calculated by subtracting row mean and diving by the s.d. for each gene across all samples, are visualized. Uninfected, $n=5$; 2 dpi, $n=4$; 4 dpi, $n=7$; 7 dpi, $n=3$; 14 dpi, $n=2$; 28 dpi, $n=2$ biologically independent mice examined over at least two independent experiments for all time points.

not as predictive of severity as other cytokines (IL6 (refs. [6,10]) and IL8 (ref. [62])) in patients but correlated with viral load[6,10]. TNFα levels in *MISTRG6-hACE2* mice were also higher early in infection with a similar but weaker correlation (Pearson's $r = 0.25$) between TNF and viral N transcript, suggesting a more pronounced role for TNFα during the acute phase of disease.

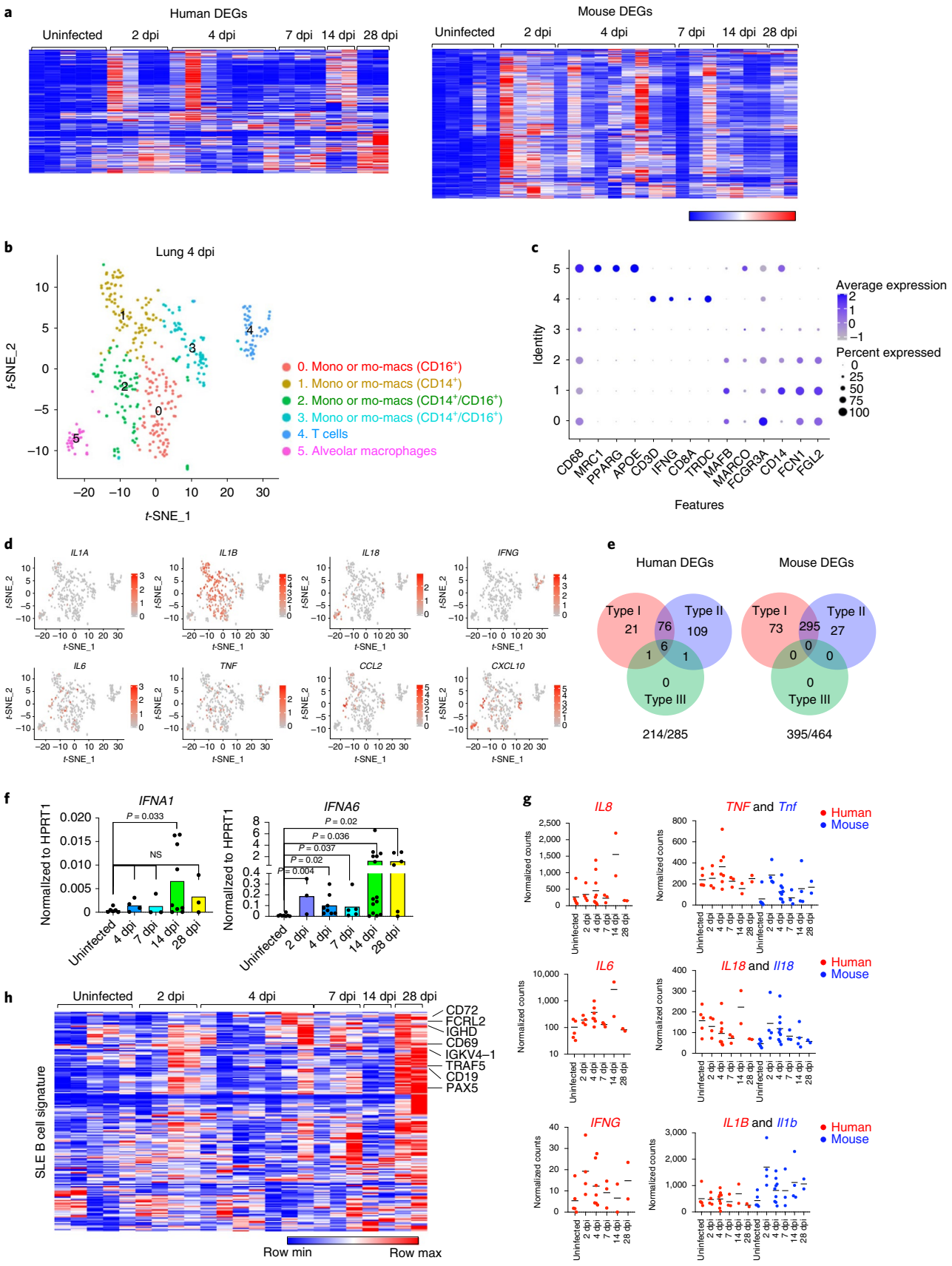

Fig. 5 | Human monoclonal recombinant antibodies as prophylactic and therapeutic interventions affect disease outcome. a, Viral titers measured by PFU in homogenized lung tissue at 4 dpi in *MISTRG6-hACE2* mice that received prophylactic treatment of convalescent patient plasma or were left untreated. Paired, two-tailed *t*-test. Untreated controls: $n = 6$ convalescent treated group and $n = 4$ biologically independent mice examined over two independent experiments. Individual values for each mouse and means are presented. **b**, Human immune cells at 4 dpi in lungs of *MISTRG6-hACE2* mice that received prophylactic treatment of convalescent patient serum or were left untreated. Paired, two-tailed *t*-test. Untreated controls: $n = 6$ convalescent treated group and $n = 4$ biologically independent mice examined over two independent experiments. Individual values for each mouse and means are presented. **c**, Human macrophages ($hCD45^+hCD68^+$) at 4 dpi in lungs of *MISTRG6-hACE2* mice that received prophylactic treatment of convalescent patient serum or were left untreated. Paired, two-tailed *t*-test. Untreated controls: $n = 6$ convalescent treated group and $n = 4$ biologically independent mice examined over two independent experiments. Individual values for each mouse and means are presented. **d**, Viral RNA and viral titers measured by PFU in homogenized lung tissue at 4 dpi in *MISTRG6-hACE2* mice that received prophylactic treatment of monoclonal antibody clone 135 (m135) or clone 144 (m144) 8 h before infection or were left untreated (untd). $n = 6$. Mann–Whitney, two-tailed test was used for comparison of viral RNA. One-sample Wilcoxon signed-rank test was used to determine significance in the viral titer quantification (effect size = 0.9, $W = 21$). **e**, Human immune cells in lungs of *MISTRG6-hACE2* mice received a prophylactic treatment of monoclonal antibody clone 135 (m135) or clone 144 (m144) 8 h before infection or were left untreated (untd). $n = 6$ biologically independent mice examined over two independent experiments. Individual values for each mouse and means are presented. Unpaired *t*-test, two-tailed. **f**, Human immune cells in BAL of *MISTRG6-hACE2* mice that received a prophylactic treatment of monoclonal antibody clone 135 (m135) or clone 144 (m144) 8 h before infection or were left untreated (untd). Untreated control $n = 4$ and treated group $n = 5$ biologically independent mice examined over two independent experiments. Individual values for each mouse and means are presented. Unpaired *t*-test, two-tailed. **g**, Human immune lineages in lungs and BAL of mAb-treated or untreated mice at 4 dpi within the human $CD45^+$ population. Classical monocytes ($CD14^+$), intermediate monocytes ($CD14^+CD16$), non-classical monocytes ($CD16^+CD14^-$), macrophages ($CD68^+$), NK cells ($NKP46^+$), T cells ($CD3^+$) and B cells ($CD19^+$ and/or $CD20^+$). *MISTRG6-hACE2* mice received a prophylactic treatment of monoclonal antibody clone 135 (m135) or clone 144 (m144) 8 h before infection or were left untreated (untd). In lungs, $n = 6$ biologically independent mice examined over three independent experiments. Individual values for each mouse and means are presented. In BAL, untreated control $n = 4$ and treated group $n = 5$ biologically independent mice examined over two independent experiments. Individual values for each mouse and means are presented. Unpaired *t*-test, two-tailed. Statistical significance was deemed by comparison to uninfected group. *P* values are represented by: NS $P > 0.05$; $^*P \leq 0.05$; $^{**}P \leq 0.01$; $^{***}P \leq 0.001$; $^{****}P \leq 0.0001$. Only changes in frequencies of lung macrophages (m135 $P = 0.029$, m144 $P = 0.037$) and BAL macrophages (m144 $P = 0.0042$) and monocytes ($CD16^+$ (m135 $P = 0.0051$, m144 $P = 0.0058$)) were statistically significant. **h**, Human macrophages ($hCD45^+hCD68^+$) at 4 dpi in lungs and BAL of *MISTRG6-hACE2* mice that received prophylactic treatment of mAbs (clone 135 or 144) or were left untreated. Lungs: untreated control $n = 6$ and treated group $n = 5$ biologically independent mice examined over three independent experiments. BAL: untreated control $n = 5$ and treated group $n = 4$ biologically independent mice examined over two independent experiments. Individual values for each mouse and means are presented. Unpaired *t*-test, two-tailed. **i**, Weight change in mAb-treated mice (prophylaxis) at 2 dpi and 4 dpi plotted as percent change compared to original weight measured just before inoculation with SARS-CoV-2. $n = 6$ biologically independent mice examined over two independent experiments. Repeated-measures one-way ANOVA with Dunnett's multiple comparison test comparing weight change at 4 dpi to untreated group was used. *P* value for m144 = 0.01 and *P* value for m135 = 0.98. Individual values for each mouse and means are presented. **j**, Viral RNA and viral titers measured by PFU in homogenized lung tissue at 4 dpi in *MISTRG6-hACE2* mice that received post-infection treatment of a mixed cocktail of monoclonal antibodies clone 135 (m135) and clone 144 (m144) or were left untreated (untd). Early treatment groups were treated at 11 hpi, and late treatment groups were treated at 35 hpi. Mann–Whitney, two-tailed test was used for comparison of viral RNA. One-sample Wilcoxon signed-rank test was used to determine significance in the viral titer quantification (effect size = 0.9, $W = 21$). Untreated control $n = 6$ and early and late treated groups $n = 5$ biologically independent mice examined over three independent experiments. Individual values for each mouse and means are presented. **k**, Human immune cells in lungs of *MISTRG6-hACE2* mice that received early, late or no treatment of monoclonal antibody mix. Untreated control $n = 6$ and early and late treated groups $n = 5$ biologically independent mice examined over three independent experiments. Individual values for each mouse and means are presented. Unpaired, two-tailed *t*-test. *P* values <0.05 are plotted. **l**, Human immune cells in BAL of *MISTRG6-hACE2* mice that received early, late or no treatment of monoclonal antibody mix. Untreated control $n = 4$ and early and late treated groups $n = 5$ biologically independent mice examined over three independent experiments. Individual values for each mouse and means are presented. Unpaired, two-tailed *t*-test. *P* values <0.05 are plotted. Untreated control $n = 6$ and early and late treated groups $n = 5$ biologically independent mice examined over three independent experiments. Individual values for each mouse and means are presented. **m**, Weight change upon mAb therapeutic treatment at 2 and 4 dpi plotted as percent change compared to original weight measured just before inoculation with SARS-Cov-2. $n = 6$ biologically independent mice examined over three independent experiments. Individual values for each mouse and means are presented. One-way ANOVA (Sidak's multiple comparisons test) comparing weight change at 4 dpi to untreated group was used. Early treatment versus untreated $P = 0.8$ and late treatment versus untreated $P = 0.49$. **n**, Human immune lineages in lungs and BAL of mAb-treated (early or late) or untreated mice at 4 dpi within the human $CD45^+$ population. Classical monocytes ($CD14^+$), intermediate monocytes ($CD14^+CD16$), non-classical monocytes ($CD16^+CD14^-$), macrophages ($CD68^+$), NK cells ($NKP46^+$), T cells ($CD3^+$) and B cells ($CD19^+$ and/or $CD20^+$). *MISTRG6-hACE2* mice were therapeutically treated with mAb mix early at 11 hpi or late at 35 hpi. Lung: untreated control $n = 6$ and early and late treated groups $n = 5$ biologically independent mice examined over three independent experiments. Individual values for each mouse and means are presented. BAL: untreated control $n = 4$ and early and late treated groups $n = 5$ biologically independent mice examined over three independent experiments. Individual values for each mouse and means are presented. Statistical significance was deemed by unpaired *t*-test compared to uninfected group. *P* values are represented by: NS $P > 0.05$; $^*P \leq 0.05$; $^{**}P \leq 0.01$; $^{***}P \leq 0.001$; $^{****}P \leq 0.0001$. Only changes in frequencies of monocytes ($CD14^+CD16^+$) were statistically significant ($P = 0.01$). Means with s.d. are plotted. In Fig. 5, MISTRG6 mice were engrafted with $CD34^+$ cells neonatally isolated from at least two donors. Pooled or infection matched representative results of at least two independent experiments are presented. Only *P* values <0.05 are shown. Mean with s.d. or individual values are plotted. N.D., not detected; NS, not significant.

Given the role of type I interferons on bystander activation of T and B cells[64,65], we first focused on the genes that typify bystander activation of memory T cells[64]. This suggested that, early in infection (2–4 dpi), T cell activation might be an antigen-independent, interferon-driven response (Extended Data Fig. 3h). We sought to identify the origin of genes upregulated in patients by validating their expression in our infected mice and then identifying their cellular source[8]. B cell response in humanized lungs was particularly enriched for genes that are upregulated in patients with moderate and severe COVID-19 (Extended Data Fig. 3i,j). Lack of germinal center formation coupled with extrafollicular B cell responses correlated with poor clinical outcomes in patients with COVID-19

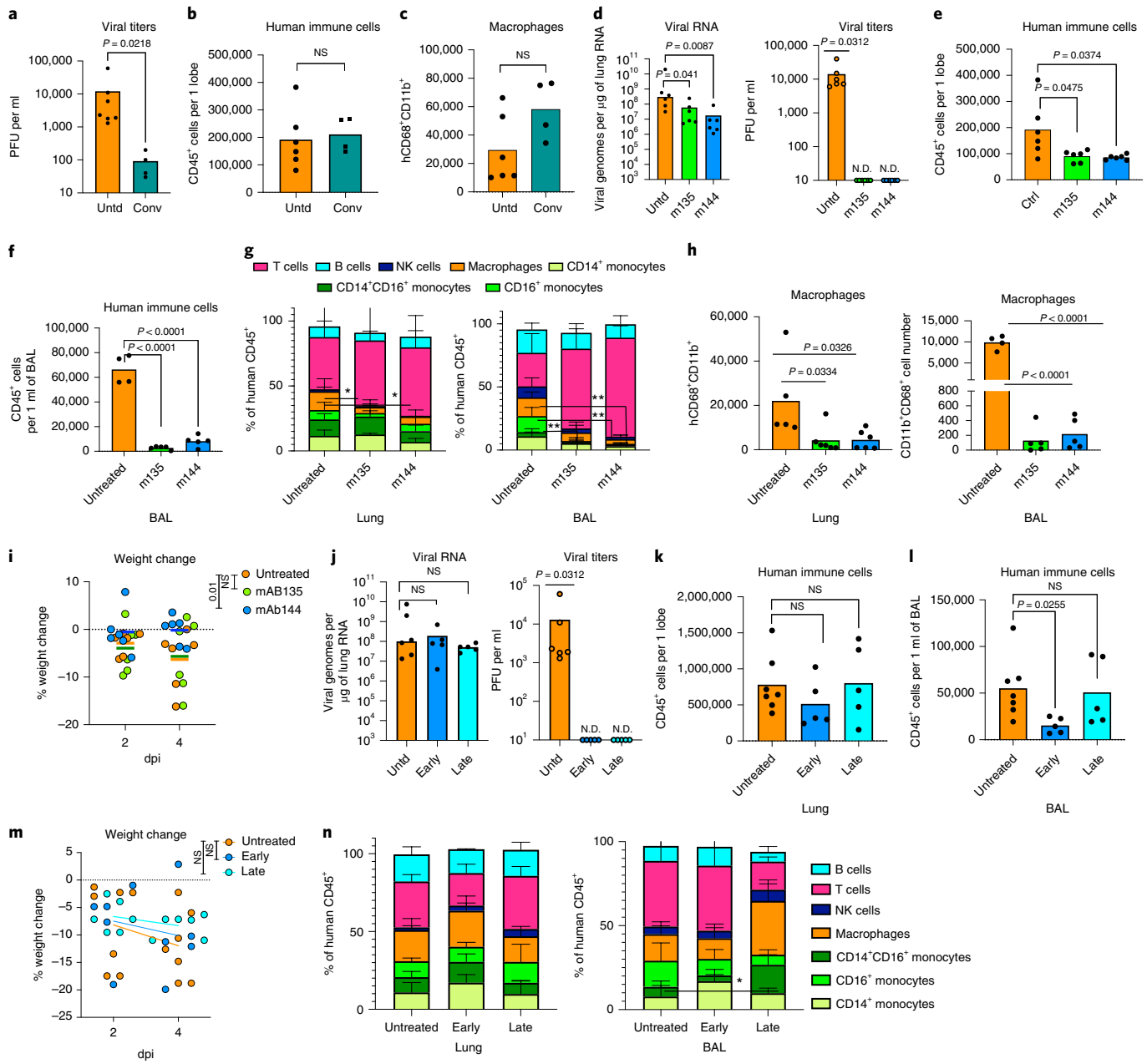

(refs. [50,66]). In line with these observations, unbiased pathway analysis of the 28-dpi lung transcriptome (Fig. 4a, Extended Data Fig. 3I and Supplementary Table 2), and a more focused look at the SLE gene signatures[67] identified a particular enrichment of SLE-like extrafollicular responses in lungs of infected mice at 28 dpi (Fig. 4h). Furthermore, B cell responses at 28 dpi exhibited the features of activated, bystander, clonal B cells that are not vaccine-specific in the context of influenza vaccine response, previously characterized in humans[65] (Extended Data Fig. 3k), further suggesting a highly inflammatory, bystander B cell response in humanized COVID-19 (refs. [8,10,11,50]). Taken together, our lung transcriptome analysis identifies a central role of monocyte-derived macrophage interferon response that persists and is amplified later in infection and suggests that interferons regulate both the innate and adaptive immune response in COVID-19.

Human monoclonal recombinant antibodies as prophylactic and therapeutic interventions affect disease outcome. We tested whether *MISTRG6-hACE2* mice could be used to evaluate patient-derived human antibodies as modulators of infection. *MISTRG6-hACE2* mice were treated with convalescent plasma[68] before infection with SARS-CoV-2 (Extended Data Fig. 4a). The treated mice had significantly lower viral titers in lungs at 4 dpi, showing that the plasma was partially effective (Fig. 5a). However, prophylactic convalescent plasma did not prevent weight loss or histopathological transition into the organizing phase, highlighted by immune cell infiltration, particularly inflammatory macrophages, into the alveolar spaces (Fig. 5b,c and Extended Data Fig. 4b,c) These findings highlight the limited efficacy of prophylactic administration of convalescent plasma in controlling lung pathology[69–71]. Monoclonal recombinant antibodies (mAbs) cloned from these convalescent patients had high neutralizing activity against SARS-CoV-2 in vitro and in vivo[68,72]. Thus, we tested two complementary mAb clones in vivo for prophylactic and therapeutic treatments of SARS-CoV-2 infection in humanized mice (Extended Data Fig. 4a,i). Mice were treated either with individual mAbs

before infection or with both mAbs combined at two time points after infection (11 or 35 hours post-infection (hpi)) and analyzed at 4 dpi (Extended Data Fig. 4a,i). As measured by viral titers and viral RNA in lungs, prophylactic treatment with mAbs prevented SARS-CoV-2 infection (Fig. 5d). Prophylactic antibody administration also attenuated immune infiltration, yielding fewer infiltrating immune cells, particularly macrophages in lungs and BAL (Fig. 5e–h and Extended Data Fig. 5d). Although T cell activation in lungs was similar, possibly due to bystander activation of T cells, treatment with mAb clone-144 reduced infiltrating Tγδ cells in lungs (Extended Data Fig. 4e,f) and prevented both systemic T cell lymphopenia (Extended Data Fig. 4g,h) and weight loss (Fig. 5i). Next, we tested therapeutic mAb treatment in *MISTRG6-hACE2* mice. Although therapeutic treatment with mAbs similarly prompted viral clearance at both early and late time points, this failed to prevent immune infiltration or significantly alter the composition of the immune infiltrate in lungs in contrast to prophylaxis (Fig. 5j–n and Extended Data Fig. 4j,l,m). Humanized mice treated with both mAbs early (11 hpi) had fewer immune cells in BAL at 4 dpi compared to untreated and late (35 hpi) treated groups, suggesting that the inflammatory responses are attenuated by early treatment, but less so by late treatment, with mAbs (Fig. 5l). Although neither therapeutic intervention prevented weight loss, early treatment prevented systemic T cell lymphopenia, whereas later mAb administration had little effect and a similar infiltration profile as untreated mice at 4 dpi (Fig. 5n and Extended Data Fig. 4k–m). These findings highlight the efficacy of mAb treatment in controlling viral infection and viral titers but underline the need for early treatment to control immunopathology, as noted clinically[69–71].

Accurate timing of corticosteroids is necessary to balance viral clearance and prevent immunopathology. Our transcriptome analysis revealed glucocorticoids as possible upstream regulators of DEGs that are induced in infected lungs (Fig. 4a and Supplementary Table 2). Moreover, given that dexamethasone is, thus far, the only therapeutic treatment that has strongly affected recovery and reduced mortality in patients with severe disease[73], we hypothesized that dexamethasone treatment might attenuate immunopathology in mice infected with SARS-CoV-2. To test this hypothesis, we treated mice with dexamethasone for 3 d starting at 7 dpi, when the immune infiltration is established but viral titers had declined in lungs (Extended Data Fig. 5a). Mice treated with dexamethasone recovered weight rapidly by 14 dpi and resumed weight gain similar to their uninfected counterparts (Figs. 1d and 6a). Dexamethasone treatment reduced human immune infiltration and reversed immune activation (Fig. 6b–i). Mouse neutrophils in BAL were fewer in dexamethasone-treated mice (Extended Data Fig. 5b), and inflammatory macrophages were largely absent from dexamethasone-treated mouse lungs (Fig. 6c–f). Alveolar macrophages were restored after therapy to a frequency similar to uninfected animals (Fig. 6e,f). Dexamethasone also blocked accumulation of pDCs (Fig. 6g) and reduced T cell activation in lungs (Fig. 6h,i and Extended Data Fig. 5c). Interestingly, dexamethasone treatment also blocked IgG-specific, but not IgM-specific, B cell responses (Extended Data Fig. 5d,e). It was notable that lack of immune cells in dexamethasone-treated lungs also correlated with lower viral RNA levels by 28 dpi (Extended Data Fig. 5f). As the immune infiltrate is established early (by 4 dpi), we investigated the timing of dexamethasone-mediated control of immunopathology for COVID-19. We treated mice early with dexamethasone for 3 d starting at 3 dpi once the immune infiltration was established and viral titers were still high (Extended Data Fig. 5g). In stark contrast to late treatment, early dexamethasone-treated mice became moribund by 7 dpi with rapidly declining weights compared to untreated

Fig. 6 | Accurate timing of corticosteroids is necessary to balance viral clearance and prevent immunopathology. a, Weight change in dexamethasone-treated or control untreated mice during SARS-CoV-2 infection plotted as percent change compared to original weight before viral inoculation. Mice were treated with dexamethasone at 7, 8 and 9 dpi. Untreated $n = 8$ and treated $n = 6$ biologically independent mice examined over three independent experiments. Unpaired, two-tailed *t*-test determined comparing 14-dpi values ($P = 0.0041$). Means with s.d. are plotted. **b**, Human immune cells in 14-dpi lungs and BAL of *MISTRG6-hACE2* mice treated with dexamethasone at 7, 8 and 9 dpi or left untreated. Untreated $n = 8$ and treated $n = 6$ biologically independent mice examined over three independent experiments. Unpaired, two-tailed *t*-test. Individual values for each mouse and means are plotted. **c**, Human immune lineages in 14 dpi-lungs of dexamethasone-treated or untreated mice within the human CD45$^+$ population. Classical monocytes (CD14$^+$), intermediate monocytes (CD14$^+$CD16), non-classical monocytes (CD16$^+$CD14$^-$), macrophages (CD68$^+$), NK cells (NKP46$^+$), T cells (CD3$^+$) and B cells (CD19$^+$ and/or CD20$^+$). *MISTRG6-hACE2* mice were treated with dexamethasone at 7, 8 and 9 dpi. Unpaired, two-tailed *t*-test. Untreated $n = 6$ and treated $n = 5$ biologically independent mice examined over three independent experiments. Means with s.d. are plotted. **d**, Number of human macrophages in lungs of dexamethasone-treated and untreated mice at 14 dpi. Unpaired, two-tailed *t*-test. Untreated $n = 8$ and treated $n = 5$ biologically independent mice examined over three independent experiments. Individual values for each mouse and means are plotted. **e**, Frequencies of alveolar or inflammatory macrophages in the lungs of *MISTRG6-hACE2* mice that were treated with dexamethasone or left untreated. Unpaired, two-tailed *t*-test. Untreated $n = 7$ and treated $n = 5$ biologically independent mice examined over three independent experiments. Individual values for each mouse and means are plotted. **f**, Numbers of alveolar or inflammatory macrophages in the lungs of *MISTRG6-hACE2* mice that were treated with dexamethasone or left untreated. Unpaired, two-tailed *t*-test. Untreated $n = 6$ and treated $n = 5$ biologically independent mice examined over three independent experiments. Individual values for each mouse and means are plotted. **g**, Frequencies (left) and numbers (right) of pDCs at 14 dpi in the lungs of dexamethasone-treated or control mice. Unpaired, two-tailed *t*-test. Untreated $n = 5$ and treated $n = 4$ biologically independent mice examined over three independent experiments. Individual values for each mouse and means are plotted. **h**, Representative histograms for HLA-DR expression in lung T cells at 14 dpi in dexamethasone-treated or control mice. Unpaired, two-tailed *t*-test. Representative of $n = 4$ mice examined over two independent experiments. All attempts resulted in similar findings. **i**, Frequencies of HLA-DR$^+$ or ICOS$^+$ T cells at 14 dpi in the lungs and BAL of dexamethasone-treated or control mice. Unpaired, two-tailed *t*-test. Lung: untreated $n = 5$ and treated $n = 4$ biologically independent mice examined over three independent experiments. BAL: untreated $n = 4$ and treated $n = 3$ biologically independent mice examined over three independent experiments. Individual values for each mouse and means are plotted. **j**, Weight change in dexamethasone-treated or control mice during SARS-CoV-2 infection plotted as percent change compared to original weight before viral inoculation. Mice were treated with dexamethasone at 3, 4 and 5 dpi. Untreated $n = 6$ and treated $n = 4$ biologically independent mice examined over two independent experiments. Unpaired, two-tailed *t*-test. Means with s.d. are plotted. **k**, Human immune cells in lungs of *MISTRG6-hACE2* mice treated with dexamethasone at 3, 4 and 5 dpi or left untreated (ctrl). $n = 4$ biologically independent mice examined over two independent experiments. Unpaired, two-tailed *t*-test. Individual values for each mouse and means are plotted. **l**, Viral RNA and viral titers measured by PFU in homogenized lung tissue at 7 dpi in dexamethasone-treated or control mice. $n = 4$ biologically independent mice examined over two independent experiments. Unpaired, two-tailed *t*-test. Individual values for each mouse and means are plotted. Mann–Whitney test, two-tailed. MISTRG6 mice were engrafted with CD34$^+$ cells neonatally isolated from at least two donors. Pooled or infection matched representative results of at least two independent experiments are presented. Only *P* values <0.05 are plotted. Mean with s.d. or individual values are plotted. Dex, dexamethasone; Ctrl, control; NS, not significant.

mice (Fig. 6j). Dexamethasone-treated mice had significantly fewer immune cells infiltrating the lungs and lacked inflammatory macrophages (Fig. 6k and Extended Data Fig. 5h). Notably, the disabled anti-viral response in these mice led to significantly higher viral loads in the lungs (Fig. 6l). These deleterious consequences of early dexamethasone treatment highlight the importance of the early anti-viral response to contain the viral infection. Careful exploration of differential timing of dexamethasone treatment distinguishes the early protective anti-viral response and the subsequent pathological immune response.

Discussion

Here we present a humanized COVID-19 mouse model that combines vector-based delivery of hACE2 and a comprehensive human immune system that recapitulates both innate and adaptive human immunity during SARS-CoV-2 infection. Our model supports chronic disease and enables characterization of the effects of patient-derived antibodies and identification of the sources of immunopathology, in particular the aberrant macrophage response.

Limitations of our model include substantial variability between individual animals and, to a lesser degree, between cohorts. Many parameters might contribute to variability. Although each cohort is engrafted with HSPCs from the same donor, the degree of engraftment varies between individual animals, and, thus, each individual animal tested is unique in its baseline human immune system. Different cohorts are engrafted with cells from different donors; thus, there is genetic variability between different cohorts, which can be exploited in the future. In this study, we used 11 different donors as sources of HSPCs. Further variability can result from experimental differences with the amount of AAV administration and efficiency of cellular infection. Transcriptome analysis revealed differences between individual animals in the strength of the inflammatory response, which might also explain the variable outcome observed in disease outcome in human SARS-CoV-2 infection[74]. However, regardless of such heterogeneity, sustained interferon response, as has been postulated in humans[13,45,46,54], was a common theme that shaped both early anti-viral innate response and late adaptive immune response in humanized COVID-19.

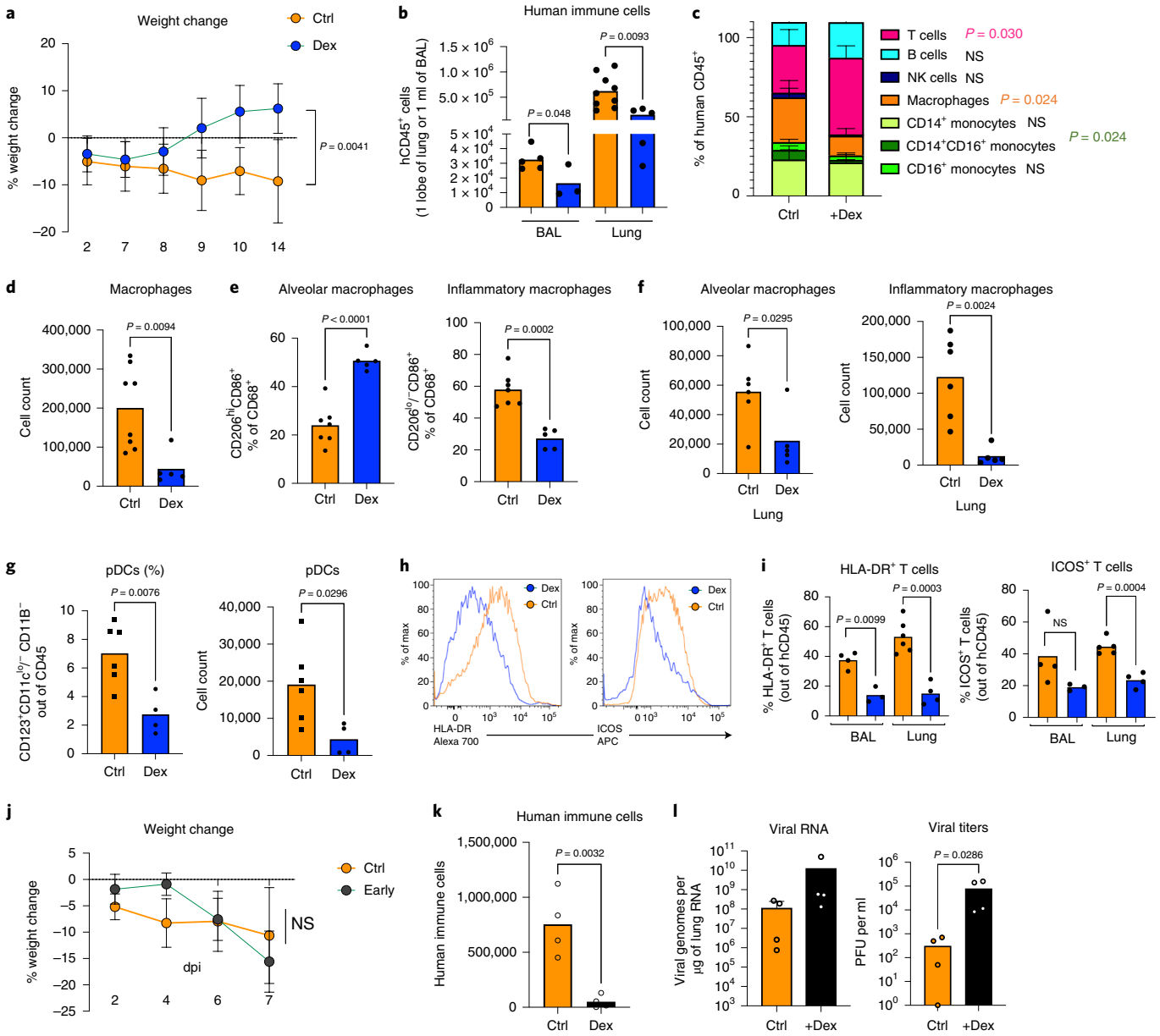

Sustained viral RNA and gross clinical features, including failure to recover body weight and severe lung pathology even at very late time points after infection, are unique among animal models to our MISTRG6 model, with human immune cells and hACE2 expression, which suggests a potentially unique contribution of human immune cells to pathology and/or viral RNA persistence. Human immune cells could produce various factors that might affect infected cells and infection dynamics or be targets of infection themselves. In human lung autopsies, SARS-CoV-2 genomes have been detected in alveolar macrophages[53], which express ACE2. We also have detected viral RNA in sorted human immune cells (hCD45$^+$), specifically in sorted hCD45$^+$CD11b$^+$ cells, enriched for human macrophages, but it is not clear whether RNA detected here is the result of viral replication or a residue of phagocytosed infected epithelial cells. Viral titers measured using sensitive cell culture systems were detectable throughout the duration of disease in engrafted *MISTRG6-hACE2* mice. Although lung sampling of viable virus is largely lacking in humans, a few patients with severe disease had positive SARS-CoV-2 culture beyond the acute 10-d window after symptom onset[75–82]. Chronic disease manifestations reflected in histopathological abnormalities (significant cellular infiltrates, thickened septa and collagen deposition) of infected humanized lungs late in infection point to lack of recovery and fibrosis, recapitulating severe human COVID-19 lung pathology. To our knowledge, no other COVID-19 disease model recapitulates the chronic weight loss, sustained high viral RNA and chronic histopathology with pulmonary fibrosis as seen in human patients (Extended Data Fig. 1)[4,14,16–19,33–35,37–39,83,84]. Nonetheless, chronic, humanized COVID-19 is not a lethal disease, which will stimulate further investigation of variables such as age, pre-existing health conditions and comorbidities that contribute to high case fatality rate in humans.

Systemic T cell lymphopenia was another common feature of humanized COVID-19 and human disease[11,12,50]. Systemic, cyclical lymphopenia that follows rapid, strong activation of T cells in the infected lungs suggest that T cells are continuously recruited, activated and consumed in the lungs of infected *MISTRG6-hACE2* mice. In matched samples, we looked for genes in the lung transcriptome that correlate with spleen T cell frequencies to link systemic lymphopenia to transcriptional changes in lungs. Frequencies of splenic T cells negatively correlated with human expression of genes such as *HIF1A*, *UBAP2L*, *MIF* and *FABP7* (Supplementary Table 4), suggesting that inflammation and stress response in lungs, possibly mediated by lung macrophages, might affect systemic lymphopenia. Genes that correlated with systemic lymphopenia were also enriched for ISGs (30/50 top correlating human genes and 26/50 top correlating mouse genes) and suggest some potential therapeutic targets to improve lymphopenia in patients.

MISTRG6-hACE2 mice allowed the study of two aspects of the immune response: infectious viral clearance and immunopathology. We first evaluated patient-derived human antibodies to study this separation. Despite efficient viral clearance, as measured by sharply reduced viral titers, and lack of antibody-mediated enhancement of disease, mAbs, when given late, did not help prevent the potentially pathological inflammatory response, suggesting that the players of immune pathology, such as the inflammatory macrophages, are recruited very early in infection. Our preclinical data are similar to the clinical experience of more than 20 SARS-CoV-2-specific monoclonal antibodies currently in different stages of clinical trial testing[69–71]. Results so far also support a reduction in viral load upon mAb treatment[69]. Notably, the antibodies prevent hospitalization and death if administered early. Our model could be particularly useful in evaluating efficacy and timing for these antibodies[71]. When administered in a timely manner, mAbs could be particularly useful in protecting uninfected individuals and preventing transmission from an infected person by rapid clearance of infectious virus.

Separating the two aspects of the immune response—infectious viral clearance and immunopathology—recapitulated in our model might prove useful in the control of COVID-19. Patients might benefit from early mAb treatment coupled with dexamethasone later in infection. Our data suggest that glucocorticoids, specifically dexamethasone (decoded as upstream regulators of the inflammatory gene signature in humanized COVID-19), should be considered only when viral titers are undetectable, suggesting that timing is crucial in promoting immune protection while preventing pathology and highlighting the importance of accurate and frequent viral detection methods. When applied to chronic disease, dexamethasone effectively controls immunopathology and reverses COVID-19 morbidity. As expected, dexamethasone treatment has broad effects and reverses many aspects of immune activation. However, non-specific suppression of the immune system using dexamethasone early in infection was catastrophic.

Even in the absence of previously described high-risk criteria, there are debilitating effects among certain COVID-19 patient groups. Although socio-economic factors might be responsible for some or all of these effects, perturbation of the proposed system should allow testing of direct medical effects. Our humanized mouse system can be completely personalized by matching patient HSPCs with antibodies and medical history, allowing the testing of novel therapeutics to address conflicting reports in pre-clinical models and to predict efficacy in patients.

Online content

Any methods, additional references, Nature Research reporting summaries, source data, extended data, supplementary information, acknowledgements, peer review information; details of author contributions and competing interests; and statements of data and code availability are available at https://doi.org/10.1038/s41587-021-01155-4.

Received: 26 February 2021; Accepted: 5 November 2021;
Published online: 17 December 2021

References

1. Letko, M., Marzi, A. & Munster, V. Functional assessment of cell entry and receptor usage for SARS-CoV-2 and other lineage B betacoronaviruses. *Nat. Microbiol.* **5**, 562–569 (2020).
2. Huang, C. et al. Clinical features of patients infected with 2019 novel coronavirus in Wuhan, China. *Lancet* **395**, 497–506 (2020).
3. Mehta, P. et al. COVID-19: consider cytokine storm syndromes and immunosuppression. *Lancet* **395**, 1033–1034 (2020).
4. Xu, Z. et al. Pathological findings of COVID-19 associated with acute respiratory distress syndrome. *Lancet Respir. Med.* **8**, 420–422 (2020).
5. Schulte-Schrepping, J. et al. Severe COVID-19 is marked by a dysregulated myeloid cell compartment. *Cell* **182**, 1419–1440 (2020).
6. Del Valle, D. M. et al. An inflammatory cytokine signature predicts COVID-19 severity and survival. *Nat. Med.* **26**, 1636–1643 (2020).
7. Liao, M. et al. Single-cell landscape of bronchoalveolar immune cells in patients with COVID-19. *Nat. Med.* **26**, 842–844 (2020).
8. Zhang, J. Y. et al. Single-cell landscape of immunological responses in patients with COVID-19. *Nat. Immunol.* **21**, 1107–1118 (2020).
9. Chua, R. L. et al. COVID-19 severity correlates with airway epithelium–immune cell interactions identified by single-cell analysis. *Nat. Biotechnol.* **38**, 970–979 (2020).
10. Lucas, C. et al. Longitudinal analyses reveal immunological misfiring in severe COVID-19. *Nature* **584**, 463–469 (2020).
11. Chen, Z. & Wherry, E. J. T cell responses in patients with COVID-19. *Nat. Rev. Immunol.* **20**, 529–536 (2020).
12. Mathew, D. et al. Deep immune profiling of COVID-19 patients reveals distinct immunotypes with therapeutic implications. *Science* **369**, eabc8511 (2020).
13. Delorey, T. M. et al. COVID-19 tissue atlases reveal SARS-CoV-2 pathology and cellular targets. *Nature* **595**, 107–113 (2021).
14. Yang, X. H. et al. Mice transgenic for human angiotensin-converting enzyme 2 provide a model for SARS coronavirus infection. *Comp. Med.* **57**, 450–459 (2007).
15. Li, W. et al. Efficient replication of severe acute respiratory syndrome coronavirus in mouse cells is limited by murine angiotensin-converting enzyme 2. *J. Virol.* **78**, 11429–11433 (2004).

16. McCray, P. B. et al. Lethal infection of K18-*hACE2* mice infected with severe acute respiratory syndrome coronavirus. *J. Virol.* **81**, 813–821 (2007).
17. Israelow, B. et al. Mouse model of SARS-CoV-2 reveals inflammatory role of type I interferon signaling. *J. Exp. Med.* **217**, e20201241 (2020).
18. Bao, L. et al. The pathogenicity of SARS-CoV-2 in hACE2 transgenic mice. *Nature* **583**, 830–833 (2020).
19. Hassan, A. O. et al. A SARS-CoV-2 infection model in mice demonstrates protection by neutralizing antibodies. *Cell* **182**, 744–753 (2020).
20. Xu, H. et al. High expression of ACE2 receptor of 2019-nCoV on the epithelial cells of oral mucosa. *Int. J. Oral. Sci.* **12**, 8–8 (2020).
21. Yan, R. et al. Structural basis for the recognition of SARS-CoV-2 by full-length human ACE2. *Science* **367**, 1444–1448 (2020).
22. Hoffmann, M. et al. SARS-CoV-2 cell entry depends on ACE2 and TMPRSS2 and is blocked by a clinically proven protease inhibitor. *Cell* **181**, 271–280 (2020).
23. Theocharides, A. P., Rongvaux, A., Fritsch, K., Flavell, R. A. & Manz, M. G. Humanized hemato-lymphoid system mice. *Haematologica* **101**, 5–19 (2016).
24. Rongvaux, A. et al. Human hemato-lymphoid system mice: current use and future potential for medicine. *Annu Rev. Immunol.* **31**, 635–674 (2013).
25. Rongvaux, A. et al. Development and function of human innate immune cells in a humanized mouse model. *Nat. Biotechnol.* **32**, 364–372 (2014).
26. Rathinam, C. et al. Efficient differentiation and function of human macrophages in humanized CSF-1 mice. *Blood* **118**, 3119–3128 (2011).
27. Willinger, T. et al. Human IL-3/GM-CSF knock-in mice support human alveolar macrophage development and human immune responses in the lung. *Proc. Natl Acad. Sci. USA* **108**, 2390–2395 (2011).
28. Strowig, T. et al. Transgenic expression of human signal regulatory protein alpha in Rag2$^{-/-}\gamma_c^{-/-}$ mice improves engraftment of human hematopoietic cells in humanized mice. *Proc. Natl Acad. Sci. USA* **108**, 13218–13223 (2011).
29. Rongvaux, A. et al. Human thrombopoietin knockin mice efficiently support human hematopoiesis in vivo. *Proc. Natl Acad. Sci. USA* **108**, 2378–2383 (2011).
30. Yu, H. et al. A novel humanized mouse model with significant improvement of class-switched, antigen-specific antibody production. *Blood* **129**, 959–969 (2017).
31. Das, R. et al. Microenvironment-dependent growth of preneoplastic and malignant plasma cells in humanized mice. *Nat. Med.* **22**, 1351–1357 (2016).
32. Sippel, T. R., Radtke, S., Olsen, T. M., Kiem, H.-P. & Rongvaux, A. Human hematopoietic stem cell maintenance and myeloid cell development in next-generation humanized mouse models. *Blood Adv.* **3**, 268 (2019).
33. Sun, S.-H. et al. A mouse model of SARS-CoV-2 infection and pathogenesis. *Cell Host Microbe* **28**, 124–133 (2020).
34. Rockx, B. et al. Comparative pathogenesis of COVID-19, MERS, and SARS in a nonhuman primate model. *Science* **368**, 1012–1015 (2020).
35. Roberts, A. et al. A mouse-adapted SARS-coronavirus causes disease and mortality in BALB/c mice. *PLoS Pathog.* **3**, e5 (2007).
36. Polak, S. B., Van Gool, I. C., Cohen, D., von der Thusen, J. H. & van Paassen, J. A systematic review of pathological findings in COVID-19: a pathophysiological timeline and possible mechanisms of disease progression. *Mod. Pathol.* **33**, 2128–2138 (2020).
37. Tian, S. et al. Pathological study of the 2019 novel coronavirus disease (COVID-19) through postmortem core biopsies. *Mod. Pathol.* **33**, 1007–1014 (2020).
38. Menter, T. et al. Postmortem examination of COVID-19 patients reveals diffuse alveolar damage with severe capillary congestion and variegated findings in lungs and other organs suggesting vascular dysfunction. *Histopathology* **77**, 198–209 (2020).
39. Barton, L. M., Duval, E. J., Stroberg, E., Ghosh, S. & Mukhopadhyay, S. Covid-19 autopsies, Oklahoma, USA. *Am. J. Clin. Pathol.* **153**, 725–733 (2020).
40. Nathan, C. Neutrophils and COVID-19: Nots, NETs, and knots. *J. Exp. Med.* **217**, e20201439 (2020).
41. Shafran, N. et al. Secondary bacterial infection in COVID-19 patients is a stronger predictor for death compared to influenza patients. *Sci. Rep.* **11**, 12703 (2021).
42. Russell, C. D. et al. Co-infections, secondary infections, and antimicrobial use in patients hospitalised with COVID-19 during the first pandemic wave from the ISARIC WHO CCP-UK study: a multicentre, prospective cohort study. *Lancet Microbe* **2**, e354–e365 (2021).
43. Baharom, F. et al. Dendritic cells and monocytes with distinct inflammatory responses reside in lung mucosa of healthy humans. *J. Immunol.* **196**, 4498–4509 (2016).
44. Villani, A. C. et al. Single-cell RNA-seq reveals new types of human blood dendritic cells, monocytes, and progenitors. *Science* **356**, eaah4573 (2017).
45. Zhou, Z. et al. Heightened innate immune responses in the respiratory tract of COVID-19 patients. *Cell Host Microbe* **27**, 883–890 (2020).
46. Nienhold, R. et al. Two distinct immunopathological profiles in autopsy lungs of COVID-19. *Nat. Commun.* **11**, 5086 (2020).
47. Tan, L. et al. Lymphopenia predicts disease severity of COVID-19: a descriptive and predictive study. *Signal Transduct. Target. Ther.* **5**, 33 (2020).
48. Wang, S. et al. IL-21 drives expansion and plasma cell differentiation of autoreactive CD11c^{hi} T-bet^{+} B cells in SLE. *Nat. Commun.* **9**, 1758 (2018).
49. Jenks, S. A. et al. Distinct effector B cells induced by unregulated toll-like receptor 7 contribute to pathogenic responses in systemic lupus erythematosus. *Immunity* **49**, 725–739 (2018).
50. Woodruff, M. C. et al. Extrafollicular B cell responses correlate with neutralizing antibodies and morbidity in COVID-19. *Nat. Immunol.* **21**, 1506–1516 (2020).
51. Schultheiß, C. et al. Next-generation sequencing of T and B cell receptor repertoires from COVID-19 patients showed signatures associated with severity of disease. *Immunity* **53**, 442–455 (2020).
52. Stephens, D. S. & McElrath, M. J. COVID-19 and the path to immunity. *JAMA* **324**, 1279–1281 (2020).
53. Grant, R. A. et al. Circuits between infected macrophages and T cells in SARS-CoV-2 pneumonia. *Nature* **590**, 635–641 (2021).
54. Dolan, M. E. et al. Investigation of COVID-19 comorbidities reveals genes and pathways coincident with the SARS-CoV-2 viral disease. *Sci. Rep.* **10**, (2020).
55. Rodero, M. P. et al. Detection of interferon alpha protein reveals differential levels and cellular sources in disease. *J. Exp. Med.* **214**, 1547–1555 (2017).
56. Peiffer-Smadja, N. & Yazdanpanah, Y. Nebulised interferon beta-1a for patients with COVID-19. *Lancet Resp. Med.* **9**, 122–123 (2021).
57. Davoudi-Monfared, E. et al. A randomized clinical trial of the efficacy and safety of interferon β-1a in treatment of severe COVID-19. *Antimicrob. Agents Chemother.* **64**, e01061-20 (2020).
58. Acharya, D., Liu, G. & Gack, M. U. Dysregulation of type I interferon responses in COVID-19. *Nat. Rev. Immunol.* **20**, 397–398 (2020).
59. Blanco-Melo, D. et al. Imbalanced host response to SARS-CoV-2 drives development of COVID-19. *Cell* **181**, 1036–1045 (2020).
60. McNab, F., Mayer-Barber, K., Sher, A., Wack, A. & O'Garra, A. Type I interferons in infectious disease. *Nat. Rev. Immunol.* **15**, 87–103 (2015).
61. Major, J. et al. Type I and III interferons disrupt lung epithelial repair during recovery from viral infection. *Science* **369**, 712–717 (2020).
62. Huang, W. et al. The inflammatory factors associated with disease severity to predict COVID-19 progression. *J. Immunol.* **206**, 1597–1608 (2021).
63. Leisman, D. E. et al. Cytokine elevation in severe and critical COVID-19: a rapid systematic review, meta-analysis, and comparison with other inflammatory syndromes. *Lancet Respir. Med.* **8**, 1233–1244 (2020).
64. Low, J. S. et al. Tissue-resident memory T cell reactivation by diverse antigen-presenting cells imparts distinct functional responses. *J. Exp. Med.* **217**, e20192291 (2020).
65. Horns, F., Dekker, C. L. & Quake, S. R. Memory B cell activation, broad anti-influenza antibodies, and bystander activation revealed by single-cell transcriptomics. *Cell Rep.* **30**, 905–913 (2020).
66. Kaneko, N. et al. Loss of Bcl-6-expressing T follicular helper cells and germinal centers in COVID-19. *Cell* **183**, 143–157 (2020).
67. Hutcheson, J. et al. Combined deficiency of proapoptotic regulators Bim and Fas results in the early onset of systemic autoimmunity. *Immunity* **28**, 206–217 (2008).
68. Davide, F. R. et al. Convergent antibody responses to SARS-CoV-2 in convalescent individuals. *Nature* **584**, 437–442 (2020).
69. Cruz-Teran, C. et al. Challenges and opportunities for antiviral monoclonal antibodies as COVID-19 therapy. *Adv. Drug Deliv. Rev.* **169**, 100–117 (2020).
70. Casadevall, A. & Pirofski, L.-A. The convalescent sera option for containing COVID-19. *J. Clin. Invest.* **130**, 1545–1548 (2020).
71. Chen, P. et al. SARS-CoV-2 neutralizing antibody LY-CoV555 in outpatients with Covid-19. *N. Engl. J. Med.* **384**, 229–237 (2020).
72. Schäfer, A. et al. Antibody potency, effector function, and combinations in protection and therapy for SARS-CoV-2 infection in vivo. *J. Exp. Med.* **218**, e20201993 (2020).
73. RECOVERY Collaborative Group et al. Dexamethasone in hospitalized patients with Covid-19. *N. Engl. J. Med.* **384**, 693–704 (2020).
74. Ware, L. B. Physiological and biological heterogeneity in COVID-19-associated acute respiratory distress syndrome. *Lancet Respir. Med.* **8**, 1163–1165 (2020).
75. Singanayagam, A. et al. Duration of infectiousness and correlation with RT–PCR cycle threshold values in cases of COVID-19, England, January to May 2020. *Euro. Surveill.* **25**, 2001483 (2020).
76. Arons, M. M. et al. Presymptomatic SARS-CoV-2 infections and transmission in a skilled nursing facility. *N. Engl. J. Med.* **382**, 2081–2090 (2020).
77. Basile, K. et al. Cell-based culture of SARS-CoV-2 informs infectivity and safe de-isolation assessments during COVID-19. *Clin. Infect. Dis.* **73**, e2952–e2959 (2020).
78. Decker, A. et al. Prolonged SARS-CoV-2 shedding and mild course of COVID-19 in a patient after recent heart transplantation. *Am. J. Transpl.* **20**, 3239–3245 (2020).

79. Folgueira, M. D., Luczkowiak, J., Lasala, F., Pérez-Rivilla, A. & Delgado, R. Prolonged SARS-CoV-2 cell culture replication in respiratory samples from patients with severe COVID-19. *Clin. Microbiol. Infect.* **27**, 886–891 (2021).
80. Jeong, H. W. et al. Viable SARS-CoV-2 in various specimens from COVID-19 patients. *Clin. Microbiol. Infect.* **26**, 1520–1524 (2020).
81. Liu, W. D. et al. Prolonged virus shedding even after seroconversion in a patient with COVID-19. *J. Infect.* **81**, 318–356 (2020).
82. van Kampen, J. J. A. et al. Duration and key determinants of infectious virus shedding in hospitalized patients with coronavirus disease-2019 (COVID-19). *Nat. Commun.* **12**, 267 (2021).
83. Bussani, R. et al. Persistence of viral RNA, pneumocyte syncytia and thrombosis are hallmarks of advanced COVID-19 pathology. *EBioMedicine* **61**, 103104 (2020).
84. Wei, J. et al. Genome-wide CRISPR screens reveal host factors critical for SARS-CoV-2 infection. *Cell* **184**, 76–91 (2020).

Methods

Mice. MISTRG6 was generated by the Flavell laboratory by combining mice generated by this laboratory, the laboratory of Markus Manz and Regeneron Pharmaceuticals based on the *Rag2*$^{-/-}$*IL2rg*$^{-/-}$129xBalb/c background, supplemented with genes for human M-CSF, IL3, SIRPα, thrombopoietin, GM-CSF and IL6 knocked into their respective mouse loci[25,30]. MISTRG6 mice are deposited at Jackson Laboratories and made available to academic, non-profit and governmental institutions under a Yale-Regeneron material transfer agreement (already approved and agreed to by all parties). Instructions on obtaining the material transfer agreement for this mouse strain will be available along with strain information and upon reasonable request. Unconstituted MISTRG6 mice were maintained with cycling treatment with enrofloxacin in the drinking water (Baytril, 0.27 mg ml^{-1}). CD1 strain of mice acquired from Charles River Laboratories were used for cross-fostering of MISTRG6 pups upon birth to stabilize healthy microbiota. C57Bl/6 strain of mice (available at Jackson Laboratories) were used as controls for infection with SARS-CoV-2. All mice were maintained under specific pathogen-free conditions in our animal facilities (Biosafety Level (BSL) 1, 2 or 3) under our Animal Studies Committee-approved protocol. Mice were housed on a 14-h light and 10-h dark cycle maintained at 40–60% humidity and 72 °F ± 2 °F. All animal experimentations were performed in compliance with Yale Institutional Animal Care and Use Committee protocols. For SARS-CoV-2-infected mice, all procedures were performed in a BSL-3 facility with approval from the Yale Institutional Animal Care and Use Committee and Yale Environmental Health and Safety.

Transplantation of human CD34$^+$ hematopoietic progenitor cells into mice. Fetal liver samples were cut in small fragments, treated for 45 min at 37 °C with collagenase D (Roche, 200 μg ml^{-1}) and prepared into a cell suspension. Human CD34$^+$ cells were purified by performing density gradient centrifugation (Lymphocyte Separation Medium, MP Biomedicals), followed by positive immunomagnetic selection with EasySep Human CD34 Positive Selection Kit (STEMCELL Technologies). For intra-hepatic engraftment, newborn 1–3-day-old pups were injected with 20,000 human fetal liver CD34$^+$ cells in 20 μl of PBS into the liver with a 22-gauge needle (Hamilton Company). All use of human materials was approved by the Yale University Human Investigation Committee.

AAV-hACE2 administration. AAV9 encoding hACE2 was purchased from Vector Biolabs (AAV9-CMV-hACE2). Animals were anaesthetized using isoflurane. The rostral neck was shaved and disinfected. A 5-mm incision was made, and the trachea was visualized. Using a 32-gauge insulin syringe, a 50-μl injection dose of 10^{11} genomic copies per milliliter of AAV-CMV-hACE2 was injected into the trachea. The incision was closed with 4–0 Vicryl suture and/or 3M Vetbond tissue adhesive. After administration of analgesic, animals were placed in a heated cage until full recovery. Mice were then moved to BSL-3 facilities for acclimation.

SARS-CoV-2 infection. SARS-CoV-2 isolate USA-WA1/2020 was obtained from the BEI reagent repository. All infection experiments were performed in a BSL-3 facility, licensed by the State of Connecticut and Yale University. Mice were anesthetized using 20% v/v isoflurane diluted in propylene glycol. Using a pipette, 50 μl of SARS-CoV-2 (1–3 × 10^6 plaque-forming units (PFU)) was delivered intranasally.

Therapeutics. *MISTRG6-hACE2* mice received prophylactic treatment of convalescent plasma (5 ml kg^{-1}) or monoclonal antibodies at 10 mg kg^{-1} (clone 135-m135 or clone 144-m144) 8 h before infection. SARS-CoV-2-infected *MISTRG6-hACE2* mice received a mixed cocktail of monoclonal antibodies clone 135 (m135) and clone 144 (m144) at 20 mg kg^{-1} at 11 hpi for early treatment and 35 hpi for late treatment. SARS-CoV-2-infected *MISTRG6-hACE2* were treated with dexamethasone (Sigma-Aldrich) at 10 mg kg^{-1} for 3 d starting at 7 dpi.

Viral titers. Mice were euthanized in 100% isoflurane. Approximately half of the right lung lobe was placed in a bead homogenizer tube with 1 ml of PBS + 2% FBS. After homogenization, 300 μl of this mixture was placed in 1-ml TRIzol (Invitrogen) for RNA extraction and analysis. Remaining volume of lung homogenates was cleared of debris by centrifugation (3,900*g* for 10 min). Infectious titers of SARS-CoV-2 were determined by plaque assay in Vero E6 (standard) or Vero ACE2$^+$TMPRSS2$^+$ (sensitive) cells in DMEM 4% FBS and 0.6% Avicel RC-581[17]. Plaques were resolved at 48 hpi by fixing in 10% formaldehyde for 1 h followed by staining for 1 h in 0.5% crystal violet in 20% ethanol. Plates were rinsed in water to visualize plaques. Multiple dilutions of lung homogenates were used to quantify infectious titers (minimum number of plaques that can be quantified per milliliter of lung homogenate = 10).

Viral RNA analysis. RNA was extracted with the RNeasy Mini Kit (Qiagen) per the manufacturer's protocol. SARS-CoV-2 RNA levels were quantified using the Luna Universal Probe One-Step RT–qPCR kit (New England Biolabs) and US Centers for Disease Control and Prevention real-time RT–PCR primer/probe sets for 2019-nCoV_N1. For each sample, 1 ug of RNA was used.

Histology. Members of the Yale University Department of Pathology kindly provided assistance with embedding and sectioning of lung tissue. A pulmonary pathologist reviewed the slides blinded and identified immune cell infiltration and other related pathologies.

Isolation of cells and flow cytometry. All mice were analyzed at approximately 9–11 weeks of age. Single-cell suspensions were prepared from blood, spleen BAL and lung. Mice were euthanized with 100% isoflurane. BAL was performed using standard methods with a 22-gauge catheter (BD Biosciences). Blood was collected either retro-orbitally or via cardiac puncture after euthanasia. BAL was performed using standard methods with a 22-gauge catheter[85]. Lungs were harvested, minced and incubated in a digestion cocktail containing 1 mg ml^{-1} of collagenase D (Sigma-Aldrich) and 30 μg ml^{-1} of DNase I (Sigma-Aldrich) in RPMI at 37 °C for 20 min. Tissue was then filtered through a 70-μm filter. Cells were treated with ammonium chloride potassium buffer and resuspended in PBS with 1% FBS. Mononuclear cells were incubated at 4 °C with human (BD Biosciences) and mouse (Bio X Cell, BE0307) Fc block for 10 min. After washing, primary antibody staining was performed at 4 °C for 20 min. After washing with PBS, cells were fixed using 4% paraformaldehyde. For intracellular staining, cells were washed with BD permeabilization buffer and stained in the same buffer for 45 min at room temperature. Samples were analyzed on an LSRII flow cytometer (BD Biosciences). Data were analyzed using FlowJo software version 3.2 and plotted using Prism 9 version 9.2.0 (283).

Adoptive T cell transfer. Infected lungs (14 dpi) were processed as described before. Cells were stained with antibodies against human CD45, human/mouse CD11B, human CD3 and mouse CD45. Lung T cells (humanCD45$^+$, mouseCD45$^-$ and CD11B$^-$CD3$^+$cells) were sorted using a BD Aria Cell Sorter in a BSL-3 facility. Sorted T cells (10,000) were mixed with total splenocytes (10 million) and injected intravenously to unengrafted *MISTRG6-hACE2* mice. These mice were then infected as described before and analyzed at 4 dpi.

Antibodies. Antibodies against the following antigens were used:

Mouse antigens: CD45 (Clone: 30-F11), Ly6G (1A8), Ly6C (HK1.4), CD31(MEC13.3) and CD326 (G8.8).

Human antigens: CD45 (HI30), CD3 (UCHT1), CD14 (HCD14), CD16 (3G8), CD19 (HIB19), CD33 (WM53), CD20 (2H7), CD206 (15-2), CD86 (BU63), CD123 (6H6), IGM (MHM-88), IGG (M1310G05) CD163 (GHI/61), CD169 (7-239) CD68 (Y1/82A), CD11B (M1/70), CD11C (3.9), HLA-DR (LN3), CD183 (G025H7), ICOS (C398.4A), PD1 (A17188B), NKp46 (9E2), CD56(MEM-188), CD4 (OKT4), CD8 (SK1), TCRGD (B1), CCR7 (G043H7) and CD83 (HB15e). All antibodies were obtained from BioLegend, unless otherwise specified.

Details on antibodies were provided as Antigen(clone)/ Fluorochrome/ Supplier/ Catalog number/ Concentration. Mouse antigens: CD45 (30-F11) PerCP BioLegend 103130 1:200; CD45 (30-F11) FITC BioLegend 103108 1:200; CD45 (30-F11) Brilliant Violet (BV) 711 BioLegend 103147 1:400; Ly6G (1A8) APC/Cyanine7 BioLegend 127624 1:100; Ly6C (HKl.4) BV605 BioLegend 128036 1:400; CD31 (MEC13.3) APC/Cyanine7 BioLegend 102507 1:400; and CD326 (G8.8) APC/Cyanine7 BioLegend 118218 1:200.

Human antigens: CD45 (Hl30) BV605 BioLegend 304044 1:100; CD45 (Hl30) Pacific Blue BioLegend 304029 1:100; CD3 (UCHT1) PE BioLegend 300408 1:200; CD14(HCD14) APC/Cyanine7 BioLegend 325620 1:100; CD16 (3G8) PerCP BioLegend 302030 1:200; CD16(3G8) FITC BioLegend 302006 1:100; CD19 (HIB19) APC/Cyanine7 BioLegend 302218 1:100; CD19 (HIB19) Alexa Fluor 700 BioLegend 302226 1:100; CD33 (WM53) APC BioLegend 983902 1:100; CD20 (2H7) APC/Cyanine7 BioLegend 302313 1:100; CD20 (2H7) Alexa Fluor 700 BioLegend 302322 1:100; CD206 (15-2) PE BioLegend 321106 1:100; CD206 (15-2) APC BioLegend 321109 1:100; CD86 (BU63) PE/Cyanine7 BioLegend 374210 1:100; CD123 (6H6) PE BioLegend 306006 1:100; IGM (MHM-88) APC BioLegend 314510 1:100; IGM (MHM-88) APC/Cyanine7 BioLegend 314520 1:100; IGG (M1310G05) APC BioLegend 410712 1:100; IGG (M1310G05) APC/Cyanine7 BioLegend 410732 1:100; CD169 (7-239) APC BioLegend 346007 1:100; CD11B (M1/70) BV711 BioLegend 101242 1:100; CD11C(3.9) PE/Cyanine7 BioLegend 301608 1:200; HLA-DR (LN3) Alexa Fluor 700 BioLegend 327014 1:100; HLA-DR (LN3) PerCP BioLegend 327020 1:400; HLA-DR (LN3) FITC BioLegend 327005 1:100; CD183 (G025H7) PE/Cyanine7 BioLegend 353720 1:100; ICOS (C398.4A) APC BioLegend 313510 1:100; CD279-PD1 (A17188B) APC/Cyanine7 BioLegend 1:100; CD335-NKp46 (9E2) PE/Cyanine7 BioLegend 331916 1:100; CD56(MEM-188) APC BioLegend 304610 1:100; CD56 (MEM-188) Pacific Blue BioLegend 304629 1:50; CD4 (OKT4) BV711 BioLegend 317440 1:100; CD8 (SK1) Pacific Blue BioLegend 344718 1:100; CD8 (SK1) BV421 BioLegend 344748 1:200; TCRGD (B1) FITC BioLegend 331208 1:100; CD163 (GHl/61) APC BioLegend 333610 1:100; CD68 (Yl/82A) BV421 BioLegend 333828 1:200; CD83 (HB15) APC BioLegend 305311 1:100; and CCR7 (G043H7) PE/Cyanine7 BioLegend 353226 1:100. Convalescent plasma and monoclonal antibodies (clones 135 and 144) were acquired from M. Nussenzweig, as previously described[68].

Bulk whole tissue lung RNA sequencing. RNA isolated from homogenized lung tissue used for viral RNA analysis was also used for whole tissue transcriptome

analysis. Libraries were made with the help of the Yale Center for Genomic Analysis. In brief, libraries were prepared with an Illumina rRNA depletion kit and sequenced on a NovaSeq. Raw sequencing reads were aligned to the human–mouse combined genome with STAR (https://doi.org/10.1093/bioinformatics/bts635), annotated and counted with HTSeq (https://doi.org/10.1093/bioinformatics/btu638), normalized using DESeq2 (https://doi.org/10.1186/s13059-014-0550-8) and graphed using the Broad Institute Morpheus web tool. Differential expression analysis was also performed with DESeq2. For ISG identification, http://www.interferome.org was used with parameters -In Vivo, -*Mus musculus* or *Homo sapiens* -fold change up 2 and down 2. Corresponding pathway analysis of differentially expressed mouse and human genes was achieved using multiple platforms (Gene Ontology, gene set enrichment analysis and Ingenuity).

ELISA. IFNα (Sigma-Aldrich) ELISAs were performed based on manufacturer instructions using serum and BAL fluid from uninfected and infected mice. In short, Triton X-100 and RNase A were added to serum and BAL samples at final concentrations of 0.5% and 0.5 mg ml^{-1}, respectively, and incubated at room temperature for at least 1 h before use to reduce risk from any potential virus in serum and BAL. For serum IFNα levels, 20 ul of serum was used, and, for BAL IFNα levels, 100 ul of BAL fluid was used.

Gene expression. RNA from whole tissue samples was extracted with the RNeasy Mini Kit (Qiagen) per the manufacturer's protocol. RNA from sorted human immune cells (human $CD45^+$), pDCs ($CD123^{hi}$ and $CD11B^-$), macrophages and monocytes ($CD11B^+$) and rest of human immune cells ($CD123^-CD11B^-CD45^+$) was extracted using TRIzol reagent. Expression was normalized to human ACTB or HPRT1. Individual values and means were plotted. High-Capacity cDNA Reverse Transcription Kit was used to make cDNA. qRT–PCR was performed using a SYBR FAST universal qPCR kit (KAPA Biosystems). Predesigned KiCqStart primers for *IFNA1*, *IFNA2*, *IFNA6*, *IFNA8*, *IFNA14*, *IFNA21*, *IFNB*, *IFNG*, *HPRT1*, *ACE2*, *Ace2* and *Hprt1* were purchased from Sigma-Aldrich.

Single-cell RNA sequencing (10x Genomics). Single-cell suspensions from digested lungs were processed for droplet-based single-cell RNA sequencing, and 10,000 cells were encapsulated into droplets using 10x Chromium GEM technology. Libraries were prepared in-house using Chromium Next GEM Single Cell 3′ Reagent Kit version 3.1 (10x Genomics). Single-cell RNA sequencing libraries were sequenced using NovaSeq. Raw sequencing reads were processed with Cell Ranger 3.1.0 using a human–mouse combined reference to generate a gene cell count matrix. To distinguish human and mouse cells, we counted the number of human genes (nHuman) and mouse genes (nMouse) with non-zero expression in each cell and selected cells with nHuman >20 × nMouse as human cells. The count matrix of human cells and human genes was used in the downstream analysis with Seurat 3.2 (ref. [86]). Specifically, this matrix was filtered, retaining cells with more than 200 and fewer than 5,000 genes and less than 20% mitochondria transcripts. We then log-transformed each entry of the matrix by computing log (CPM/100 + 1), where CPM stands for counts per million. To visualize the cell subpopulations in two dimensions, we applied principal component analysis followed by *t*-distributed stochastic neighbor embedding (*t*-SNE), a non-linear dimension reduction method, to the log-transformed data. Graph-based clustering was then used to generate clusters that were overlaid on the *t*-SNE coordinates to investigate cell subpopulations. Marker genes for each cluster of cells were identified using the Wilcoxon test with Seurat. For the adjusted *P* values, the Bonferroni correction was used.

Statistical analysis. Unpaired or paired *t*-test was used to determine statical significance for changes in immune cell frequencies and numbers when comparing infected mice to uninfected control mice. For experiments where mice were treated with monoclonal antibodies or steroids, one-way ANOVA was used to determine statistical significance across groups, and adjusted *P* values were reported. To determine whether the viral RNA quantification was statistically significant across treatment groups or time points, the Mann–Whitney two-tailed test was used. A one-sample Wilcoxon signed-rank test was used as a non-parametric alternative to the one-sample *t*-test to determine whether the viral titer quantification of the untreated condition was significantly different from an undetectable viral load (that is, viral titer = 0). Note that our data cannot be assumed to be normally distributed. The results indicate that there is a significant difference between the untreated and mAb-treated mice (for example, early, late or prophylactic treatment). For these analyses, we also calculated the effect size (for example, $r = 0.90$ (large effect size), $V = 21$ and $P = 0.03$).

Additional information on research design is available in the Nature Research Reporting Summary linked to this article.

Reporting Summary. Further information on research design is available in the Nature Research Reporting Summary linked to this article.

Data availability

All data that support the findings of this study are available within the paper and its Supplementary Information files. The data supporting this publication are available at Figshare.com under project 'A humanized mouse model of COVID-19' (https://figshare.com/projects/A_humanized_mouse_model_of_COVID-19/125659). All 10x Genomics single-cell RNA sequencing and bulk RNA sequencing data that support the findings of this study were deposited in the Gene Expression Omnibus repository with accession code GSE186794.

References

85. Sun, F., Xiao, G. & Qu, Z. Murine bronchoalveolar lavage. *Bio. Protoc.* **7**, e2287 (2017).
86. Stuart, T. et al. Comprehensive integration ofsingle-cell data. *Cell* **177**, 1888–1902. e1821.
87. Imai, M. et al. Syrian hamsters as a small animal model for SARS-CoV-2 infection and countermeasure development. *Proc. Natl. Acad. Sci. USA* **117**, 16587–16595 (2020).
88. Dinnon, K. H. et al. A mouse-adapted model ofSARS-CoV-2 to test COVID-19 countermeasures. *Nature* **586**, 560–566 (2020).
89. Song, E. et al. Neuroinvasion of SARS-CoV-2 inhuman and mouse brain. *J. Exp. Med.* **218**, e20202135 (2021).
90. Ter Meulen, J. et al. Human monoclonal antibody asprophylaxis for SARS coronavirus infection in ferrets. *Lancet* **363**, 2139–2141 (2004).
91. Oladunni, F. S. et al. Lethality of SARS-CoV-2 infection in K18 human angiotensin-converting enzyme 2 transgenic mice. *Nat.Commun.* **11**, 6122 (2020).

Acknowledgements

The generation of the original MISTRG6 model was supported by the Bill and Melinda Gates Foundation. We thank G. Yancopoulos, D. Valenzuela, A. Murphy and W. Auerbach at Regeneron Pharmaceuticals who generated, in collaboration with our groups, the individual knock-in alleles combined in MISTRG. We thank H. Steach, M. Chiorazzi, I. Odell, E. Eynon and W. Philbrick and all the other members of the Flavell laboratory for discussions and comments; J. Alderman, C. Lieber, B. Cadugan and E. Hughes-Picard for administrative assistance; P. Ranney and C. Hughes for mouse colony management; D. Urbanos for human $CD34^+$ cell isolation; and L. Devine for help with cell sorting. E.S. is a Howard Hughes Medical Institute Fellow of the Damon Runyon Cancer Research Foundation (DRG-2316-18). This work was funded by the Howard Hughes Medical Institute (R.A.F., M.N. and A.I.). This study was also supported, in part, by National Institute of Health grants R01AI157488 (A.I.), F30CA239444 (E.S.), 2T32AI007517, K08AI163493 (B.I.), AI061093 (E.M.), AI118855 (E.M.), CA016359 (E.M.), K08 AI128043 (C.B.W.) and U01 CA260507 (S.H.), the Burroughs Wellcome Fund (C.B.W.), the Patterson Foundation (C.B.W.), a Fast Grant from Emergent Ventures at the Mercatus Center (A.I., E.S. and C.B.W.), the Mathers Foundation (A.I., C.B.W. and E.M.) and the Ludwig Family Foundation (A.I. and C.B.W.).

Author contributions

E.S. conceived the project, performed experiments, analyzed the data and wrote the manuscript. B.I. performed experiments and helped establish the model in Biosafety Level 3. H.M. preformed histopathological assessment of lung pathology, offered vital conceptual insights and aided in writing of the manuscript. J.Z. and R.Q. performed bioinformatics analysis. E.K. prepared samples for histopathological assessment. E.S. helped establish the model in Biosafety Level 3. M.N. provided monoclonal antibodies used in the study. S.H., E.M., Y.K., M.N., C.B.W. and A.I. offered vital conceptual insights, contributed to the overall interpretation of this work and aided in writing of the manuscript. R.A.F. co-conceived and supervised the project, helped interpret the work and supervised writing of the manuscript.

Competing interests

R.A.F. is an advisor to GlaxoSmithKline, Zai Lab and Ventus Therapeutics.

Additional information

Extended data is available for this paper at https://doi.org/10.1038/s41587-021-01155-4.

Supplementary information The online version contains supplementary material available at https://doi.org/10.1038/s41587-021-01155-4.

Correspondence and requests for materials should be addressed to Richard A. Flavell.

Peer review information *Nature Biotechnology* thanks the anonymous reviewers for their contribution to the peer review of this work.

Disease parameter	Human COVID-19	Humanized COVID-19	COVID-19 in animal models
Weight loss	>5% of initial body weight	Chronic 10-30% of initial body weight, sustained for weeks	Acute Hamsters [87]: 10% weight loss, recovers in 10 days Mouse adapted SARS-2 virus in mice[88] :10- 20 % weight loss, recovers in ~10 days
Duration of disease pathology	Weeks to months [2]	>4 weeks	4-10 days
Mortality	0.1% to over 25% case fatality rate based on age, risk factors and country	None detected	Fatal encephalitis in mouse brain upon vector mediated, transient ACE2 expressing model[89], or transgenic K18-ACE2[91]
Lung pathology	Chronic Diffuse alveolar damage, perivenular, fibrosis in severe cases [20, 37, 38, 39]	Chronic Diffuse alveolar damage, signs of fibrosis with significant cellular infiltrate late in disease	Acute: Vector-mediated or transgenic mouse models [17, 19, 33]: Mild alveolitis , peribronchiolar lymphocytic inflammation, epithelial damage Ferrets[90]: mostly upper respiratory disease with infiltration in alveolar spaces Mouse adapted SARS-2 virus in mice[88]: Acute lung injury, resolves in days
Lymphopenia	T cell lymphopenia (CD8+ T cell in particular)[2, 12, 47]	T cell lymphopenia (CD8+ T cell in particular)	None
Macrophage response	Monocytic, inflammatory macrophages as drivers of pathology [7, 8]	Monocytic, inflammatory macrophages as drivers of pathology	Monocytes and monocytic macrophages infiltrate the lungs but immunopathology resolves [17]
Cytokines	Increased levels of proinflammatory cytokines/chemokines : IL6, TNF, IL1B, IFNγ, MCP-1-CCL2, CXCL10 and others [7, 8, 10, 12]	Increased levels of proinflammatory cytokines (IL6, TNF, IL1B, IFNγ, MCP1,CXCL10 and others)	Increased levels of proinflammatory cytokines (IL6, TNF, IL1B, IFNγ, MCP1 and others) particularly in mouse adapted version of SARS-2 (ref. [17, 88])
T cell response	Activated T cells with TCR diversity correlating with better prognosis [10, 11, 12]	Activated T cells	Activated T cells [17]
IFN signature	Sustained for weeks	Sustained for weeks	Sustained for days, responsible for recruitment of Macs[89]
B cell response	Defect in germinal centers [66], extrafollicular [50], highly inflammatory [10, 11]	Extrafollicular, highly inflammatory	Germinal center response [91]
Therapeutics (Dexamethasone, Abs)	Dexamethasone [73]: reduced mortality Convalescent and monoclonal Abs [69, 70, 71]: limited response but promotes viral clearance	Dexamethasone: timing is crucial to limit immunopathology Convalescent and mAbs: beneficial as prophylactics and after early administration, late administration provides no benefit, limited response, viral titers reduced or cleared at 4dpi in all applications	Transfer of neutralizing antibodies and mAb stop disease[19]

Extended Data Fig. 1 | Comparison of COVID-19 parameters and response to therapeutics in human patients, humanized mice and other animal models. Although substantial anti-viral immunity mediates viral clearance in non-severe COVID-19[2], robust inflammatory cytokine production, decreased circulating lymphocytes and failure to generate germinal centers characterizes the immunopathology in severe COVID-19[2-4]. Dysregulated myeloid[5-8] and lymphocyte[9-12,53] compartments, including monocytes, macrophages, neutrophils, NK cells and antibody secreting B cells, have been described as players in the observed lung immunopathology of COVID-19. Accurate model systems are essential to rapidly evaluate promising discoveries but most models currently available in mice, ferrets and hamsters do not recapitulate sustained immunopathology described in COVID-19 patients. The following table summarizes various aspects of the human disease and how well these are recapitulated in existing animal models of COVID-19 and in our humanized mouse model of COVID-19. Additional work cited: refs. [87–91].

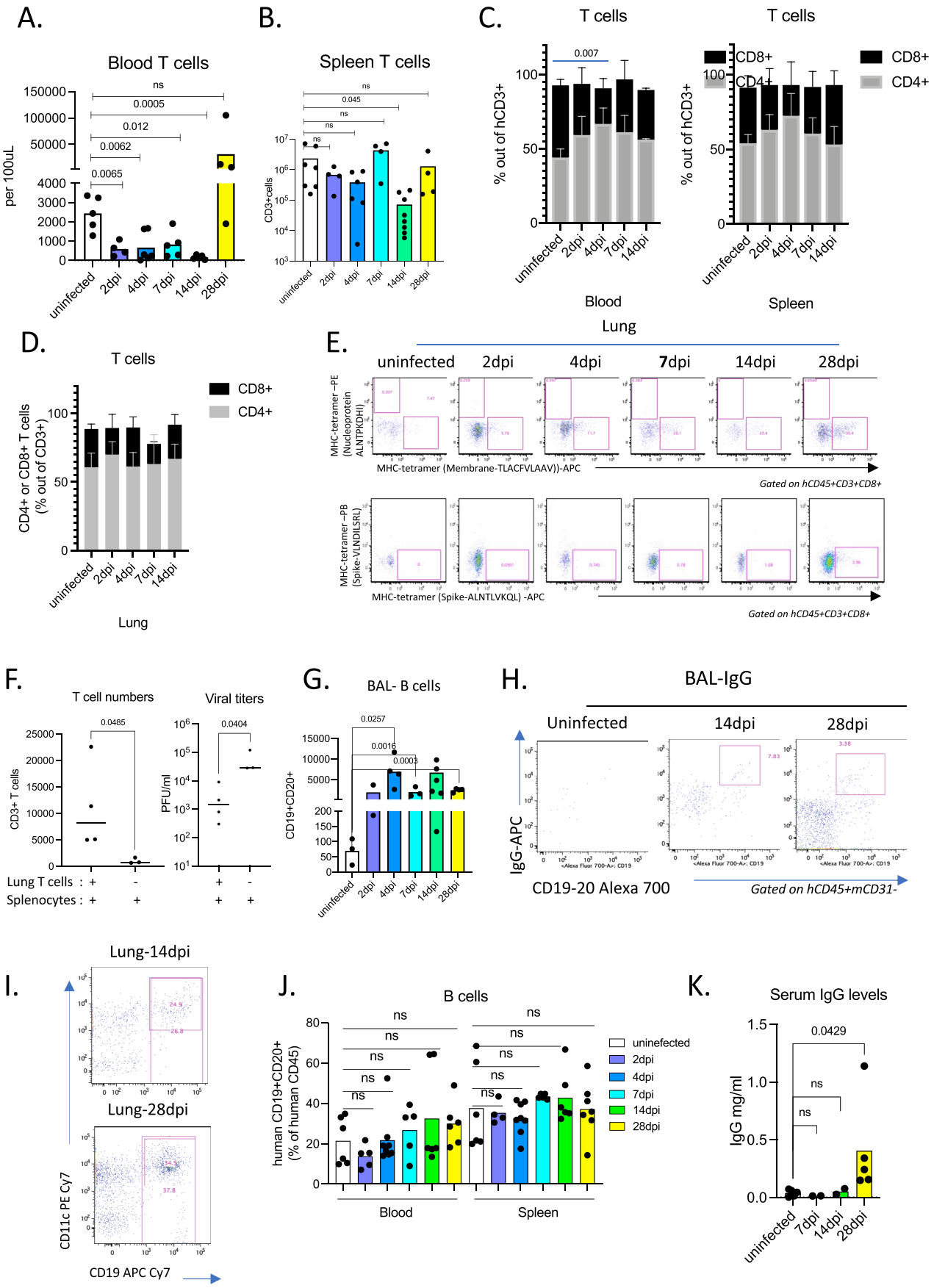

Extended Data Fig. 2 | See next page for caption.

Extended Data Fig. 2 | (matched to Fig. 3). a. Numbers of human T cells in the blood pre- and post-infection (2,4,7,14,28dpi). Unpaired, two-tailed t-test. P-values<0.05 are plotted. Uninfected n=5, 2dpi n=4, 4dpi n=6, 7dpi n=5, 14dpi n=5, 28dpi=4, biologically independent mice examined over at least 3 independent experiments. Individual values for each mouse and means are plotted. **b**. Numbers of human T cells in the spleens of uninfected or infected mice (2,4,7,14,28dpi). Unpaired, two-tailed t-test. P-values<0.05 are plotted. Unpaired, two-tailed t-test. Only p-values<0.05 are plotted. Uninfected n=7, 2dpi n=4, 4dpi n=6, 7dpi n=4, 14dpi n=8, 28dpi n=4, biologically independent mice examined over at least 3 independent experiments. Individual values for each mouse and means are plotted. **c**. Frequencies of human CD4+ or CD8+ T cells within hCD3+ population in the blood and spleens of uninfected or infected mice at 2,4,7,14,28 dpi. Blood: n=4 biologically independent mice examined over at least 2 independent experiments. Means with SD are plotted. Spleen: Uninfected n=5, 2dpi n=4, 4dpi n=6, 7dpi n=4, 14dpi n=4 biologically independent mice examined over at least 3 independent experiments. Individual values for each mouse and means are plotted. **d**. Frequencies of human CD4+ or CD8+ T cells within hCD3+ population in the lungs of uninfected or infected mice at 2,4,7,14,28 dpi. Uninfected n=4, 2dpi n=4, 4dpi n=6, 7dpi n=4, 14dpi n=4 biologically independent mice examined over 3 independent experiments. Individual values for each mouse and means are plotted. **e**. Representative flow cytometry plots of CD8+ T cells stained with viral antigen bearing HLA-A2 tetramers. HLA-A2 tetramers bound to peptides of Nucleoprotein(N), Membrane protein(M) and Spike protein were used to characterize T cells from uninfected and infected (2,4,7,14,28dpi) mice. Representative of uninfected n=3, 2dpi n=2, 4dpi n=3, 7dpi n=3, 14dpi n=3, 28dpi n=3 biologically independent mice examined over 2 independent experiments. **f**. Lung T cell numbers (per lobe) and viral titers following prophylactic T cell transfer in infected mice at 4dpi. Splenocytes and sorted T cells from lungs of 14dpi mice where the contribution of the antigen specific B cell response was minimal were transferred to unengrafted MISTRG-hACE2 (no human immune cells prior to transfer). Control MISTRG-hACE2 mice received splenocytes but not sorted lung T cells (n=3 biologically independent mice examined over 2 independent experiments). These mice were subsequently infected and analyzed at 4dpi for viral titers and human immune cells in lungs. In mice that received sorted lung T cells, human immune compartment in lungs comprised of T cells and few CD16+ monocytes and macrophages but no B cells (n=4 biologically independent mice examined over 2 independent experiments). **g**. Numbers of human B cells in the BAL of uninfected or infected mice at 2, 4, 7, 14, 28 dpi. Unpaired, two-tailed t-test. P-values<0.05 are plotted. Uninfected n=3, 2dpi n=3, 4dpi n=4, 7dpi n=3, 14dpi n=7, 28dpi n=4 biologically independent mice examined over at least 3 independent experiments. Individual values for each mouse and means are plotted. **h**. Representative flow cytometry plots of IgG+ B cells in the BAL of uninfected and infected mice 14 and 28dpi. Representative of n=4 biologically independent mice examined over 3 independent experiments. **i**. CD11C and CD19 expression on human immune cells from infected lungs at 14 and 28 dpi. Representative of n=5 (14dpi) and n=4 (28dpi) biologically independent mice examined over at least 3 independent experiments. **j**. Frequencies of human B cells marked by CD19 and CD20 expression within hCD45+ population in spleen and blood of uninfected or infected mice at 2, 4, 7, 14, 28 dpi. Blood: Uninfected n=6, 2dpi n=5, 4dpi n=8, 7dpi n=5, 14dpi n=6, 28dpi n=6 biologically independent mice examined over at least 3 independent experiments. Spleen: Uninfected n=6, 2dpi n=4, 4dpi n=8, 7dpi n=5, 14dpi n=6, 28dpi n=7 biologically independent mice examined over at least three independent experiments. Individual values for each mouse and means are plotted. **k**. IgG levels measured by ELISA in serum of uninfected or infected mice at 7, 14, 28 dpi. Uninfected n=5, 7dpi n=2, 14dpi n=2, 28dpi n=5 biologically independent mice examined over 2 independent experiments. Individual values for each mouse and means are plotted. Unpaired, two tailed t-test.

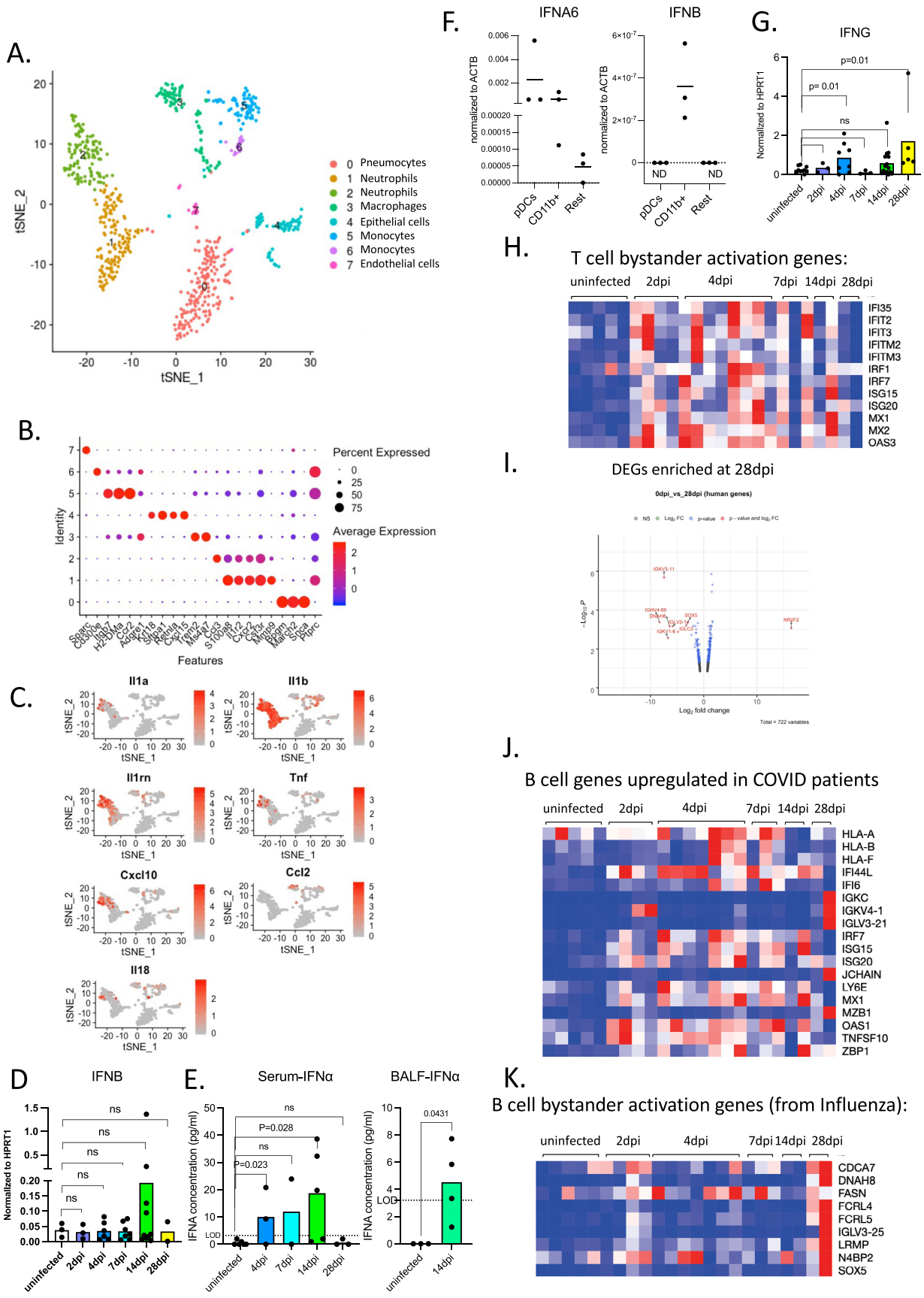

Extended Data Fig. 3 | See next page for caption.

Extended Data Fig. 3 | (matched to Fig. 4). a. t-distributed stochastic neighbor embedding (*t*-SNE) plot with clustering results of single cell RNA sequencing of mouse cells from lungs at 4dpi. Single cell suspensions from whole infected lung at 4dpi were processed and sequenced. There were 731 cells identified as mouse cells. **b**. Dot plot of cluster identifying genes for mouse cell clusters described in S4A. **c**. Cluster distribution and expression profile of mouse inflammatory cytokines for clusters described in 4B. **d**. Normalized expression of human IFNB measured by qPCR in homogenized lung tissue of uninfected and infected (2,4,7,14,28dpi) mice. Expression was normalized to human HPRT1. Unpaired t-test, one-tailed since the distribution is expected to be one-sided. Uninfected n=3, 2dpi n=3, 4dpi n=6, 7dpi n=7, 14dpi n=10, 28dpi n=2 biologically independent mice examined over at least 3 independent experiments. Individual values for each mouse and means are presented. P-values<0.05 are plotted. **e**. IFNA levels measured by ELISA in serum and BAL of uninfected or infected mice. Serum: Uninfected n=6, 4dpi n=3, 7dpi n=2, 14dpi n=5, 28dpi n=3; BAL: Uninfected n=3, 14dpi n=4 biologically independent mice examined over at least 2 independent experiments for all time points. Individual values (average of duplicates) for each mouse and means are plotted. **f**. Type I interferon levels (IFNA6 and IFNB) per cell measured by qPCR in sorted human immune cells (human CD45+): plasmacytoid dendritic cells (PDCs; CD123^{hi} CD11B-), macrophages and monocytes (CD11B+) and rest of human immune cells (CD123-CD11B-CD45+). Expression was normalized to human ACTB. Individual values and means are plotted. n=3 biologically independent mice examined over 2 independent experiments. Individual values with means are plotted. **g**. Normalized expression of human IFNG measured by qPCR in homogenized lung tissue of uninfected and infected (2,4,7,14,28dpi) mice. Expression was normalized to human HPRT1. Unpaired t-test, one tailed since distribution is expected to be one-sided. Uninfected n=10, 2dpi n=3, 4dpi n=8, 7dpi n=3, 14dpi n=15, 28dpi n=5 biologically independent mice examined over at least 3 independent experiments for all time points. **h**. Heat map of normalized counts for bystander activated memory T cell signature genes[64] (based on Low et al., JEM 2020) in lungs of MISTRG6-hACE2 mice infected with SARS-CoV-2. Row min and max of transformed values, calculated by subtracting row mean and diving by STD for each gene across all samples, are visualized. Uninfected n=5, 2dpi n=4, 4dpi n=7, 7dpi n=3, 14dpi n=2, 28dpi n=2 biologically independent mice examined over at least 2 independent experiments for all time points. **i**. Volcano plot showing foldchange and adjusted p-values (by Wald test using DESeq2) of differentially regulated genes at 28dpi compared to uninfected lungs. Genes with FC(Log2)>1 and p value<0.05 are highlighted in red. Replicates of at least 2 mice. Uninfected n=5, 28dpi n=2 biologically independent mice examined over 2 independent experiments. **j**. Heatmap of normalized counts for genes that are induced in B cells of patients with moderate or severe COVID-19 in comparison with healthy controls. Normalized counts in lungs of uninfected or infected MISTRG6-hACE2 were plotted over the course of infection. Row min and max of transformed values, calculated by subtracting row mean and diving by STD for each gene across all samples, are visualized. Uninfected n=5, 2dpi n=4, 4dpi n=7, 7dpi n=3, 14dpi n=2, 28dpi n=2 biologically independent mice examined over at least 2 independent experiments for all time points. **k**. Heatmap of normalized counts for bystander activated memory B cell signature genes[65] (based on Horns et al., 2020) in lungs of MISTRG6-hACE2 mice infected with SARS-CoV-2. Row min and max of transformed values, calculated by subtracting row mean and diving by STD for each gene across all samples, are visualized. Uninfected n=5, 2dpi n=4, 4dpi n=7, 7dpi n=3, 14dpi n=2, 28dpi n=2 biologically independent mice examined over at least 2 independent experiments for all time points.

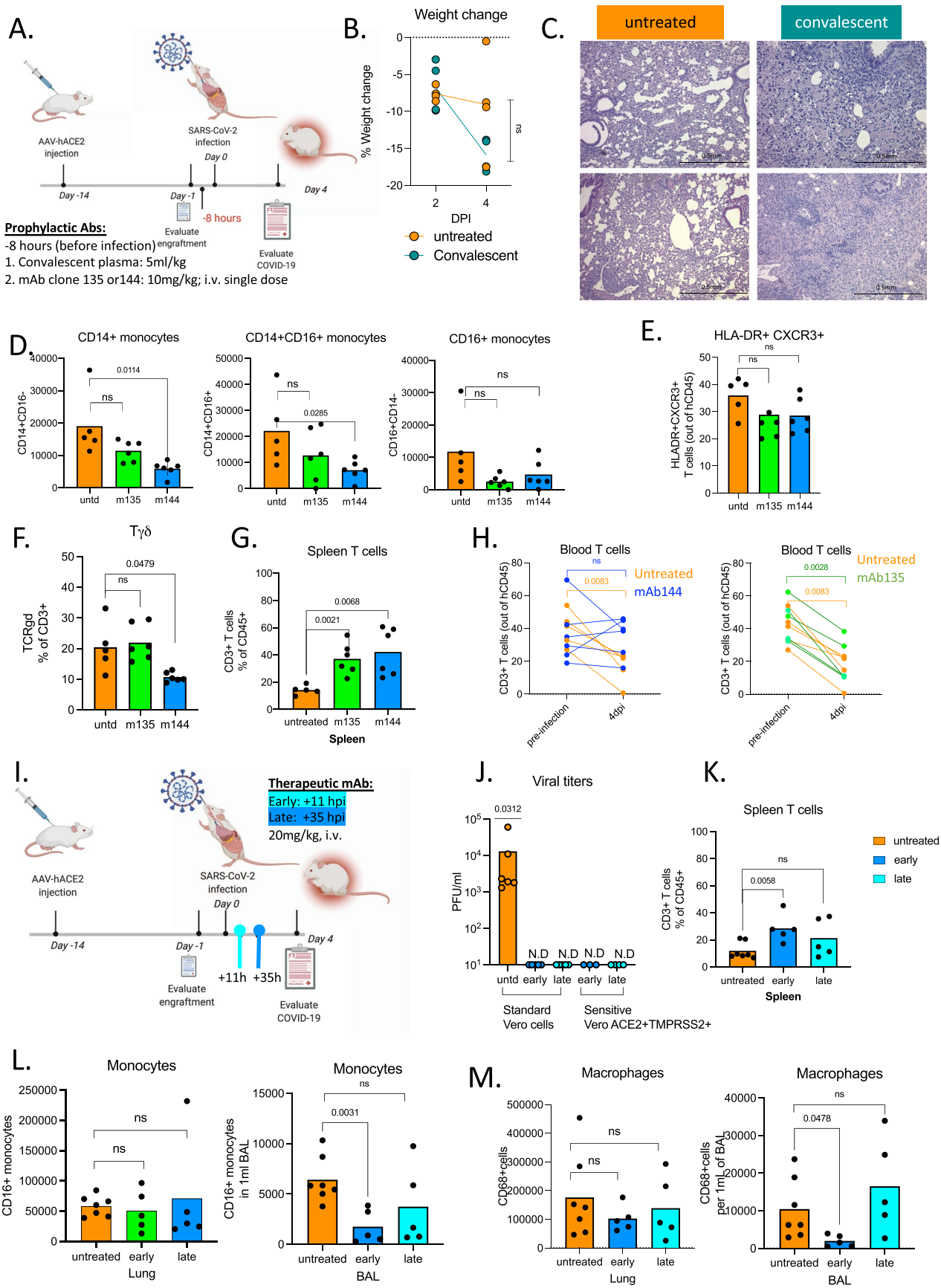

Extended Data Fig. 4 | See next page for caption.

Extended Data Fig. 4 | (matched to Fig. 5). a. Schematic of experimental design of prophylactic antibody treatment MISTRG6-hACE2 mice received prophylactic treatment of convalescent plasma (5ml/kg) or monoclonal antibodies at 10mg/kg (clone 135 -m135 or clone 144-m144) 8 h prior to infection or left untreated (untd). Mice were euthanized 4dpi. Convalescent plasma samples from the top 30 neutralizers in a cohort of 148 individuals were pooled to create a mixture with an NT50 titer of 1597 against HIV-1 pseudotyped with SARS-CoV-2 S protein[68]. Sequencing the antibody genes from infected humans has revealed the expansion of closely related Receptor Binding Domain of the Spike protein (RBD)-specific B cell antibody clones in different SARS-CoV-2 infected individuals. Although most convalescent plasma samples obtained from patients who recovered from COVID-19 did not contain high levels of neutralizing activity, RBD-specific antibodies with potent antiviral activity were found in all individuals tested[68]. Monoclonal recombinant antibodies (mAbs) used in this study were cloned from these convalescent patients and had high neutralizing activity against SARS-CoV-2 *in vitro* and *in vivo* in mouse adapted SARS-CoV-2 infection[68,72]. **b**. Weight change in convalescent plasma treated mice at 2 and 4dpi plotted as percent change compared with original weight measured just before inoculation with SARS-CoV-2. Unpaired t-test, two-tailed comparing 4dpi values. N=4 biologically independent mice examined over 2 independent experiments for all time points. Individual values per each mouse plotted. **c**. Representative images (10x magnification) of H&E staining of lungs (4dpi) from mice treated prophylactically with convalescent plasma or left untreated. The histopathological findings mark transition into the organizing phase, highlighted by infiltration of the inter- and intra-alveolar space by lymphocytes macrophages, and fibroblasts. Representative of N=4 biologically independent mice examined over 2 independent experiments for all time points. Individual values for each mouse are plotted. **d**. Frequencies of human monocytes (CD14+ classical; CD14+CD16+ intermediate, CD16+ non classical) within human CD45+ cells in the lungs of MISTRG6-hACE2 mice which received a prophylactic treatment of monoclonal antibody clone 135 (m135) or clone 144(m144) 8 h prior to infection or left untreated (untd). Unpaired, two-tailed t-test. P-values<0.05 are plotted. Untreated N=5, treated n=6 biologically independent mice examined over 2 independent experiments for all time points. Individual values for each mouse and means are plotted. **e**. Frequencies of HLA-DR+CXCR3+ T cells within human CD3+CD45+ cells in lungs of MISTRG6-hACE2 mice which received a prophylactic treatment of monoclonal antibody clone 135 (m135) or clone 144(m144) 8 h prior to infection or left untreated (untd). Unpaired, two-tailed t-test. P-values<0.05 are plotted. Untreated N=5, treated n=6 N=4 biologically independent mice examined over 2 independent experiments for all time points. Individual values for each mouse and means are plotted. **f**. Frequencies of Tγδ cells within human CD3+CD45+ cells in lungs of MISTRG6-hACE2 mice which received prophylactic treatment of monoclonal antibody clone 135 (m135) or clone 144(m144) 8 h prior to infection or left untreated (untd). Unpaired, two-tailed t-test. N=5-6. P-values<0.05 are plotted. Untreated N=5, treated n=6 biologically independent mice examined over 2 independent experiments for all time points. Individual values for each mouse and means are plotted. **g**. Frequencies of human T cells within human CD45+ cells in spleens of MISTRG6-hACE2 mice received a prophylactic treatment of monoclonal antibody clone 135 (m135) or clone 144(m144) 8 h prior to infection or left untreated (untd). Unpaired, two-tailed t-test. P-values<0.05 are plotted. Untreated N=5, treated n=64 biologically independent mice examined over two independent experiments for all time points. Individual values for each mouse and means are plotted. **h**. Frequencies of human CD3+ T cells within human CD45+ population in the blood pre- and post-infection (2, 4, 7, 14,2 8dpi). Lines connect pre- and post-infection values for the same mouse. MISTRG6-hACE2 mice received a prophylactic treatment of monoclonal antibody clone 135 (m135) or clone 144(m144) 8 h prior to infection or left untreated (untd). Paired, two-tailed t-test. P-values<0.05 are plotted. Untreated n=5, treated n=6 biologically independent mice examined over 2 independent experiments for all time points. Individual values for each mouse are plotted. **i**. Schematic of experimental design of post-infection mAb treatment. MISTRG6-hACE2 mice received a mixed cocktail of monoclonal antibodies clone 135 (m135) and clone 144(m144) at 20mg/kg or left untreated (untd). Early treatment groups were treated 11 h post-infection and late treatment 35 h post-infection. Monoclonal recombinant antibodies (mAbs) used in this study were cloned from the convalescent patients (whose plasma was used prophylactically before) and had high neutralizing activity against SARS-CoV-2 *in vitro* and *in vivo* in mouse adapted SARS-CoV-2 infection[68,72]. **j**. Viral titers measured by PFU in homogenized lung tissue following early or late therapeutic mAb at 4dpi using Vero E6 (standard assay) or Vero-ACE2+TMPRSS2+ (sensitive assay) cells. Treated n=4 biologically independent mice examined over 2 independent experiments for measurement with Vero-ACE2+TMPRSS2+ (sensitive assay) cells. Individual values for each mouse are plotted. **k**. Frequencies of human T cells within human CD45+ cells in spleens of MISTRG6-hACE2 mice that received early, late or no treatment of monoclonal antibody mix. Unpaired, two-tailed t-test. Untreated n=7, treated n=5 biologically independent mice examined over 3 independent experiments for all time points. Pooled, infection-matched mice are presented. P-values<0.05 are plotted. Individual values representing each mouse are plotted. Individual values for each mouse are plotted. **l**. Number of CD16+ human monocytes in lungs of treated and untreated mice at 4dpi. Mice were either MISTRG6-hACE2 mice that received a mixed cocktail of monoclonal antibodies clone 135 (m135) and clone 144(m144) or left untreated (untd). Early treatment group was treated 11 h post-infection (hpi) and late treatment 35 hpi. Unpaired, two-tailed t-test. Untreated n=7, treated n=5 biologically independent mice examined over 3 independent experiments for all time points. Pooled, infection-matched mice are presented. P-values<0.05 are plotted. Individual values representing each mouse are plotted. **m**. Number of human macrophages in lungs of treated and untreated mice at 4dpi. MISTRG6-hACE2 mice that received a mixed cocktail of monoclonal antibodies clone 135 (m135) and clone 144(m144) or left untreated (untd). Early treatment group was treated 11 h post-infection and late treatment 35 h post-infection. Unpaired, two-tailed t-test. Untreated n=7, treated n=5 biologically independent mice examined over 3 independent experiments for all time points. Pooled, infection-matched mice are presented. P-values<0.05 are plotted. Individual values representing each mouse are plotted.

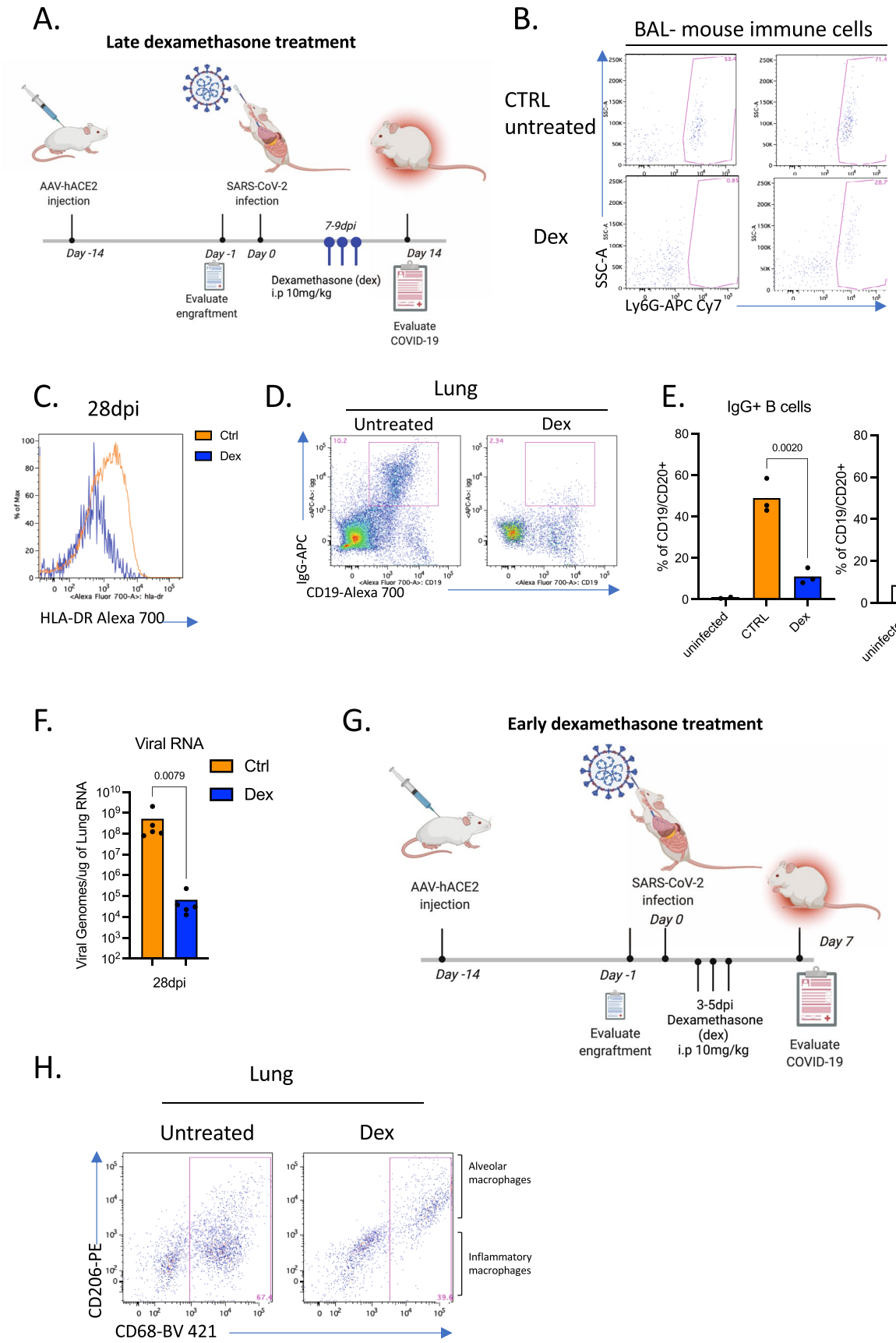

Extended Data Fig. 5 | See next page for caption.

Extended Data Fig. 5 | (matched to Fig. 6). a. Schematic of experimental design of dexamethasone treatment: SARS-CoV-2 infected MISTRG6-hACE2 mice were either treated with dexamethasone on days 7, 8, 9 post-infection or left untreated. Mice were analyzed either at 14 dpi or 28 dpi. Mice were treated intraperitoneally (i.p.) with dexamethasone at 10mg/kg dose. **b**. Representative flow cytometry plots of Ly6G expressing SSC^{hi} cells (mouse neutrophils) within the mouse immune cell population (mouse CD45+) in the BAL of dexamethasone treated or control untreated mice. Representative of 4 biologically independent mice examined over at least 2 independent experiments. **c**. HLA-DR expression on lung T cells 28 dpi in dexamethasone treated or control mice. Representative of 3 biologically independent mice examined over at least 2 independent experiments. **d**. Representative flow cytometry plots of Surface IgG and CD19 expression on human immune cells gated on hCD45+ cells in lungs of untreated or dexamethasone treated mice at 28 dpi. N=3 of biologically independent mice examined over at least 2 independent experiments. **e**. Frequencies of IgM+ and IgG+ B cells in lungs of untreated or dexamethasone treated mice at 28 dpi. Mice were treated with dexamethasone on days 7,8,9 post-infection. N=3 biologically independent mice examined over at least 2 independent experiments. Unpaired t-test, two-tailed. **f**. Viral RNA in the lung homogenates of dexamethasone treated or control untreated mice at 28dpi. Mann-Whitney, two-tailed test. N=5 biologically independent mice examined over 3 independent experiments. **g**. Schematic of experimental design of SARS-CoV-2 infected MISTRG6-hACE2 mice either treated with dexamethasone on days 3, 4, 5 dpi or left untreated. **h**. CD206 and CD68 expression in lung human immune cells in mice treated with dexamethasone or left untreated at 7dpi. CD206hi+CD68+ cells are alveolar macrophages. Treated N=4, untreated N=6 biologically independent mice examined over 2 independent experiments. Alveolar macrophages are marked by high CD206 expression. Inflammatory macrophages are enriched in the CD206 negative population which also express CD86 (not shown).

nature research

Corresponding author(s): Richard A. Flavell

Last updated by author(s): Nov 1st, 2021

Reporting Summary

Nature Research wishes to improve the reproducibility of the work that we publish. This form provides structure for consistency and transparency in reporting. For further information on Nature Research policies, see our Editorial Policies and the Editorial Policy Checklist.

Statistics

For all statistical analyses, confirm that the following items are present in the figure legend, table legend, main text, or Methods section.

n/a	Confirmed	
☐	☒	The exact sample size (*n*) for each experimental group/condition, given as a discrete number and unit of measurement
☐	☒	A statement on whether measurements were taken from distinct samples or whether the same sample was measured repeatedly
☐	☒	The statistical test(s) used AND whether they are one- or two-sided *Only common tests should be described solely by name; describe more complex techniques in the Methods section.*
☒	☐	A description of all covariates tested
☐	☒	A description of any assumptions or corrections, such as tests of normality and adjustment for multiple comparisons
☐	☒	A full description of the statistical parameters including central tendency (e.g. means) or other basic estimates (e.g. regression coefficient) AND variation (e.g. standard deviation) or associated estimates of uncertainty (e.g. confidence intervals)
☐	☒	For null hypothesis testing, the test statistic (e.g. *F*, *t*, *r*) with confidence intervals, effect sizes, degrees of freedom and *P* value noted *Give P values as exact values whenever suitable.*
☒	☐	For Bayesian analysis, information on the choice of priors and Markov chain Monte Carlo settings
☒	☐	For hierarchical and complex designs, identification of the appropriate level for tests and full reporting of outcomes
☐	☒	Estimates of effect sizes (e.g. Cohen's *d*, Pearson's *r*), indicating how they were calculated

Our web collection on statistics for biologists contains articles on many of the points above.

Software and code

Policy information about availability of computer code

Data collection

Flow cytometric data was collected in BD-LSRII instrument using Diva software.

Data analysis

Single Cell RNA Sequencing 10X Genomics:
Raw sequencing reads were processed with Cell Ranger 3.1.0 using a human-mouse combined reference to generate a gene cell count matrix. To distinguish human and mouse cells, we counted the number of human genes (nHuman) and mouse genes (nMouse) with nonzero expression in each cell, and selected cells with nHuman > 20 * nMouse as human cells. The count matrix of human cells and human genes was used in the downstream analysis with Seurat 3.2 [citation: https://doi.org/10.1016/j.cell.2019.05.031]. Specifically, this matrix was filtered retaining cells with > 200 and < 5,000 genes and < 20% mitochondria transcripts. We then log transformed each entry of the matrix by computing log (CPM/100 + 1), where CPM stands for counts per million. To visualize the cell subpopulations in two dimensions, we applied principal component analysis followed by t-SNE, a nonlinear dimension reduction method, to the log-transformed data. Graph-based clustering was then used to generate clusters that were overlaid on the t-SNE coordinates to investigate cell subpopulations. Marker genes for each cluster of cells were identified using the Wilcoxon test with Seurat. For the adjusted P values the Bonferroni correction was used.

Bulk whole tissue lung RNA-sequencing:
Raw sequencing reads were aligned to the human-mouse combined genome with STAR [citation: https://doi.org/10.1093/bioinformatics/bts635], annotated and counted with HTSeq [citation: https://doi.org/10.1093/bioinformatics/btu638], normalized using DESeq2 [citation: https://doi.org/10.1186/s13059-014-0550-8], and graphed using the Broad Institute Morpheus web tool. Differential expression analysis was also performed with DESeq2. For IFN-stimulated gene identification, http://www.interferome.org was used with parameters -In Vivo, -Mus musculus or Homo sapiens -fold change up 2 and down 2. tification, http://www.interferome.org was used with parameters -In Vivo, -Mus musculus or Homo sapiens -fold change up 2 and down 2. Corresponding pathway analysis of differentially expressed mouse and human genes was achieved using multiple platforms: Gene Ontology (GO- DOI: 10.5281/zenodo.4081749 Released 2020-10-09), Gene Set Enrichment analysis (GSEA- MSigDB 7.2), Ingenuity Pathway Analysis(IPA-Version 01-16))

Flow cytometric analysis:
Data collected using BD-LSRII flow cytometer was analyzed using FlowJo version 9.3.2 and plotted using Prism 9 Version 9.2.0 (283).

For manuscripts utilizing custom algorithms or software that are central to the research but not yet described in published literature, software must be made available to editors and reviewers. We strongly encourage code deposition in a community repository (e.g. GitHub). See the Nature Research guidelines for submitting code & software for further information.

Data

Policy information about availability of data

All manuscripts must include a data availability statement. This statement should provide the following information, where applicable:

- Accession codes, unique identifiers, or web links for publicly available datasets
- A list of figures that have associated raw data
- A description of any restrictions on data availability

All data that support the findings of this study are available within the paper and its supplementary Information files. All 10x Genomics single cell RNA sequencing and bulk RNA sequencing data that support the findings of this study are deposited in the Gene Expression Omnibus (GEO) repository with an accession codes: xxx.
Figures that have associated raw data:
1. GSE186794-(Bulk RNA sequencing: Figure 4 and Extended data figure 4, Extended data tables 2-5; single cell RNA sequencing: Figure 4 and Extended data figure 4.
We have also deposited our datasets at FIgshare under the project name: A humanized mouse model of COVID-19 https://figshare.com/account/home#/projects/125659. Two items under this project focus on 1. characterization of immune cells (10.6084/m9.figshare.16909450) and 2. gene expression analysis (10.6084/m9.figshare.16909453).

Field-specific reporting

Please select the one below that is the best fit for your research. If you are not sure, read the appropriate sections before making your selection.

☒ Life sciences ☐ Behavioural & social sciences ☐ Ecological, evolutionary & environmental sciences

For a reference copy of the document with all sections, see nature.com/documents/nr-reporting-summary-flat.pdf

Life sciences study design

All studies must disclose on these points even when the disclosure is negative.

Sample size	MISTRG6 mice transplanted with fetal liver derived CD34+ cells were infected (referred as livermates when engrafted with the same donor cells) or left as uninfected controls. Sample size was chosen based on variability seen in our model in previous studies which initially described the MISTRG humanized mouse model system (doi.org/10.1038/nbt.2858) and characterized it in various contexts (DOI: 10.1126/science.abe2485) Whenever possible a minimum of 8 mice per sample per mouse strain were transplanted to account for attrition due to low humanization. For immune-reconstitution human CD34+ from 11 donors were used. Whenever possible littermates were transplanted with CD34+ cells from the same donor. In cases when litter sizes were small, multiple litters were combined and transplanted with the same donor cells (referred as livermates) and were cross-fostered by the same nursing CD1 mother. All qRT-PCRs were performed in duplicates with at least 3 biologic replicates.
Data exclusions	Humanized mice which had lower than 30% humanization in blood were not included in the study or data collection. In lung transcriptomic analysis, whole tissue lung samples with less than 1% human reads were excluded from analysis. These criteria were preestablished based on our prior experience working with humanized mouse tissues.
Replication	All experiments described were repeated at least two times, mostly three or four times with matching littermate and livermate controls. These matched controls were carried for across infection time points or control and treated groups. All attempts of replication were successful.
Randomization	Mice with humanization comparable (+/- 10% of mean) humanization value (% of human immune cells/ total immune cells) in blood were included in control vs treated groups. All these mice had >30% humanization at 8 weeks post-engraftment.
Blinding	All histopathological assessment and scoring of H&E and trichrome stained slides were performed on blinded samples by a board certified pathologist. Experimenters were not blinded to group allocation during sample collection of flow cytometric studies but were blinded during data analysis. For all other assays experimenters were blinded to group allocation for both data collection and analysis.

Reporting for specific materials, systems and methods

We require information from authors about some types of materials, experimental systems and methods used in many studies. Here, indicate whether each material, system or method listed is relevant to your study. If you are not sure if a list item applies to your research, read the appropriate section before selecting a response.

Materials & experimental systems

n/a	Involved in the study
☐	☒ Antibodies
☐	☒ Eukaryotic cell lines
☒	☐ Palaeontology and archaeology
☐	☒ Animals and other organisms
☒	☐ Human research participants
☒	☐ Clinical data
☒	☐ Dual use research of concern

Methods

n/a	Involved in the study
☒	☐ ChIP-seq
☐	☒ Flow cytometry
☒	☐ MRI-based neuroimaging

Antibodies

Antibodies used

Antibodies against the following antigens were used:
Mouse antigens (clone)/ Fluorochrome/ Supplier/ Catalogue number/ Concentration
CD45 (30-F11) PerCP Biolegend 103130 1:200
CD45 (30-F11) FITC Biolegend 103108 1:200
CD45 (30-F11) Brilliant Violet (BV) 711 Biolegend 103147 1:400
Ly6G (1A8) APC/Cyanine7 Biolegend 127624 1:100
Ly6C (HKl.4) BV605 Biolegend 128036 1:400
CD31(MEC13.3) APC/Cyanine7 Biolegend 102507 1:400
CD326 (G8.8) APC/Cyanine7 Biolegend 118218 1:200
Human antigens(clone) Fluorochrome Supplier Cat # Concentration
CD45(HI30) BV605 Biolegend 304044 1:100
CD45(HI30) Pacific Blue Biolegend 304029 1:100
CD3(UCHT1) PE Biolegend 300408 1:200
CD14(HCD14) APC/Cyanine7 Biolegend 325620 1:100
CD16(3G8) PerCP Biolegend 302030 1:200
CD16(3G8) FITC Biolegend 302006 1:100
CD19(HIB19) APC/Cyanine7 Biolegend 302218 1:100
CD19(HIB19) Alexa Fluor 700 Biolegend 302226 1:100
CD33(WM53) APC Biolegend 983902 1:100
CD20(2H7) APC/Cyanine7 Biolegend 302313 1:100
CD20(2H7) Alexa Fluor 700 Biolegend 302322 1:100
CD206(15-2) PE Biolegend 321106 1:100
CD206(15-2) APC Biolegend 321109 1:100
CD86(BU63) PE/Cyanine7 Biolegend 374210 1:100
CD123(6H6) PE Biolegend 306006 1:100
IGM(MHM-88) APC Biolegend 314510 1:100
IGM(MHM-88) APC/Cyanine7 Biolegend 314520 1:100
IGG(M1310G05) APC Biolegend 410712 1:100
IGG(M1310G05) APC/Cyanine7 Biolegend 410732 1:100
CD169(7-239) APC Biolegend 346007 1:100
CD11B(M1/70) BV711 Biolegend 101242 1:100
CD11C(3.9) PE/Cyanine7 Biolegend 301608 1:200
HLA-DR(LN3) Alexa Fluor 700 Biolegend 327014 1:100
HLA-DR(LN3) PerCP Biolegend 327020 1:400
HLA-DR(LN3) FITC Biolegend 327005 1:100
CD183(G025H7) PE/Cyanine7 Biolegend 353720 1:100
ICOS(C398.4A) APC Biolegend 313510 1:100
CD279-PD1(A17188B) APC/Cyanine7 Biolegend 1:100
CD335-NKp46(9E2) PE/Cyanine7 Biolegend 331916 1:100
CD56(MEM-188) APC Biolegend 304610 1:100
CD56(MEM-188) Pacific Blue Biolegend 304629 1:50
CD4{OKT4) BV711 Biolegend 317440 1:100
CD8(SK1) Pacific Blue Biolegend 344718 1:100
CD8(SK1) BV421 Biolegend 344748 1:200
TCRGD(B1) FITC Biolegend 331208 1:100
CD163(GHI/61) APC Biolegend 333610 1:100
CD68(YI/82A) BV421 Biolegend 333828 1:200
CD83(HB15) APC Biolegend 305311 1:100
CCR7(G043H7) PE/Cyanine7 Biolegend 353226 1:100

Convalescent plasma and monoclonal antibodies (clone 135 and 144) were acquired from M. Nussenzweig

Validation

All antibodies used in this study are commercially available, and all have been validated by the manufacturers and used by other publications. Likewise, we titrated these antibodies based on requirements of our samples. The following were validated in the following species:
Antibody (clone)/ Source/ Reactivity
CD45 (30-F11) -Biolegend- mouse
Ly6G (1A8) -Biolegend- mouse

Ly6C (HKl.4) -Biolegend- mouse
CD31(MEC13.3) -Biolegend- mouse
CD326 (G8.8) -Biolegend- mouse
CD45 (Hl30) -Biolegend- Human, Chimpanzee
CD3 (UCHT1) -Biolegend- Human, Chimpanzee
CD14 (HCD14) -Biolegend- Human
CD16 (3G8) -Biolegend- Human, African Green, Baboon, Capuchin Monkey, Chimpanzee, Cynomolgus, Marmoset, Pigtailed Macaque, Rhesus, Sooty Mangabey, Squirrel Monkey
CD19 (HIB19) -Biolegend- Human, Chimpanzee, Rhesus
CD33 (WM53) -Biolegend- Human
CD20 (2H7) -Biolegend- Human
CD206 (15-2) -Biolegend- Human
CD86 (BU63) -Biolegend- Human
CD123(6H6) -Biolegend- Human, Rhesus
IGM (MHM-88) -Biolegend- Human, African Green, Baboon, Cynomolgus, Rhesus
IGG(M1310G05) -Biolegend- Human
CD169(7-239) -Biolegend- Human
CD11B (M1/70) -Biolegend- Mouse, Human, Chimpanzee, Baboon, Cynomolgus, Rhesus, Rabbit
CD11C (3.9) -Biolegend- Human, African Green, Baboon, Chimpanzee, Cynomolgus, Rhesus, Squirrel Monkey
HLA-DR(LN3) -Biolegend- Human, Rhesus
CD183 (G025H7) -Biolegend- Human, African Green, Baboon, Cynomolgus, Rhesus
ICOS(C398.4A) -Biolegend- Human, African Green, Baboon, Cynomolgus, Mouse, Rat, Rhesus, Swine
CD279 -PD1 () -Biolegend- Human
CD335-NKp46 (9E2) -Biolegend- Human
CD56(MEM-188) -Biolegend- Human, Cattle, Swine
CD4{OKT4) -Biolegend- Human, Chimpanzee, Cynomolgus, Rhesus
CD8(SK1) -Biolegend- Human, African Green, Chimpanzee, Cynomolgus, Pigtailed Macaque, Rhesus, Sooty Mangabey
TCRGD(B1) -Biolegend- Human, African Green, Baboon, Cynomolgus, Pigtailed Macaque, Rhesus
CD163 (GHl/61) -Biolegend- Human, African Green, Cynomolgus, Rhesus
CD68(Yl/82A) -Biolegend- Human
CD83(HB15) -Biolegend- Human, African Green, Baboon, Pigtailed Macaque, Rhesus
CCR7(G043H7) -Biolegend- Human, African Green, Baboon, Cynomolgus, Rhesus

Eukaryotic cell lines

Policy information about cell lines

Cell line source(s)	VERO C1008 (Vero 76, clone E6, Vero E6) were obtained from ATCC. Vero ACE2+ TMPRSS2+ cells were obtained from B. Graham (NIAID).
Authentication	None of the cell lines were authenticated
Mycoplasma contamination	Cell lines were not tested for mycoplasma contamination
Commonly misidentified lines (See ICLAC register)	No commonly misidentified cell lines were used in the study.

Animals and other organisms

Policy information about studies involving animals; ARRIVE guidelines recommended for reporting animal research

Laboratory animals	The studies described here involve the engraftment of human hematopoietic stem and progenitor cells in immunocompromised MISTRG6 mice. MISTRG6 was generated by R. Flavell based on the Rag2-/- IL2rg-/-129xBalb/c background with genes for human M-CSF, IL-3, SIRPα, thrombopoietin, GM-CSF and IL6 knocked into their respective mouse loci. CD1 strain of mice were used for cross-fostering to stabilize healthy microbiota. Mice were housed in 14 hour light and 10 hour dark cycle maintained at 40-60% humidity and 72 degrees F +/- 2 degrees. All of the animals in this project were housed in the animal care facility at Yale University School of Medicine under appropriate biosafety level conditions (1,2,3). These facilities are specifically designed for this purpose and are administered by the Departments of Comparative Medicine according to National Institutes of Health guidelines.
Wild animals	The study did not involve wild animals.
Field-collected samples	The study does not involve field-collected samples.
Ethics oversight	Departments of Comparative Medicine according to National Institutes of Health guidelines; Institutional Animal Care and Use Committee (IACUC).

Note that full information on the approval of the study protocol must also be provided in the manuscript.

Flow Cytometry

Plots

Confirm that:

☒ The axis labels state the marker and fluorochrome used (e.g. CD4-FITC).

☒ The axis scales are clearly visible. Include numbers along axes only for bottom left plot of group (a 'group' is an analysis of identical markers).

☒ All plots are contour plots with outliers or pseudocolor plots.

☒ A numerical value for number of cells or percentage (with statistics) is provided.

Methodology

Sample preparation	We have developed a comprehensively humanized mouse COVID-19 model that faithfully recapitulates the innate and adaptive human immune responses during infection with SARS-CoV-2. We achieve this by adapting recombinant adeno-associated virus (AAV)-driven gene therapy to deliver human ACE2 (hACE2) to the lungs of MISTRG6 mice and infecting these mice with SARS-Cov-2. All samples including uninfected controls were prepared in Biosafety level 3 facilities. SARS-CoV-2 infected MISTRG6-hACE2 were treated with dexamethasone (i.p.) at 10mg/kg for 3 days starting at 7dpi. Mice All mice were analyzed at approximately 9-14 weeks of age. Single cell suspensions were prepared from blood, spleen, BAL and lung. Mice were euthanized with 100% isoflurane. BAL was performed using standard methods with a 22G Catheter (BD). Blood was collected either retro-orbitally or via cardiac puncture following euthanasia. BAL was performed using standard methods with a 22G Catheter (BD)61. Lungs were harvested, minced and incubated in a digestion cocktail containing 1 mg/ml collagenase D (Sigma) and 30 µg/ml DNase I (Sigma-Aldrich) in RPMI at 37°C for 20 min. Tissue was then filtered through a 70-µm filter. Cells were treated with ammonium- chloride-potassium buffer and resuspended in PBS with 1% FBS. Mononuclear cells were incubated on ice with human (BD) and mouse (BioXcell, BE0307) Fc block for 10 min. After washing, surface antibody staining was performed at 4C for 20 min. After washing with PBS, cells were fixed using 4% paraformaldehyde. For intracellular staining, cells were washed with BD permeabilization buffer and stained in the same buffer for 45 min at room temperature. Samples were analyzed on an LSRII flow cytometer (BDBiosciences). RNA isolated from homogenized lung tissue used for viral RNA analysis was also used for whole tissue transcriptome analysis. Libraries were made with the help of the Yale Center for Genomic Analysis. Briefly, libraries were prepared with an Illumina rRNA depletion kit and sequenced on a NovaSeq. Single cell suspensions from digested lungs were processed for droplet based scRNA-seq and 10000 cells were encapsulated into droplets using 10X Chromium GEM technololgy. Libraries were prepared in house using Chromium Next GEM Single Cell 3' Reagent Kits v3.1 (10X Genomics). scRNA-seq libraries were sequenced using Nova-Seq 6000.
Instrument	BD LSRII (with yellow-green laser), 10x Chromium, NovaSeq, BD ARIA cell sorter
Software	FlowJo 9.3.2 version; Morpheus (https://software.broadinstitute.org/morpheus); Prism v9.2.0.
Cell population abundance	Post-sort populations achieved over 95% purity assessed by resorting of a small representative aliquot.
Gating strategy	Cells were analyzed using 6 different staining panels based on the cells of interest. Cells were gated on live cells as shown in Fig S2. Human immune cells within the live gate were selected by excluding mouse CD45+ and including human CD45+ cells. Macrophages were gated by CD68, CD11b and high HLA-DR co-expression. Alveolar macrophages were identified by high expression of CD206 and CD86. All macrophages expressed high levels of CD169. Inflammatory macrophages had low or no expression of CD206 but expressed high levels of CD86 within the CD68+ population. Monocytes were gated within CD68 negative gate and identified based on expression of CD14 and/or CD16. T cells were gated based on CD3+ expression within human immune cells. Activation and polarization of T cells were measured by HLA-DR, ICOS, PD-1, CXCR3 expression within CD3+ cells. TCR gamma/delta T cells were identified by TCR gamma/delta expression within CD3+ cells. NK cells were gated based on CD56 and/or NKP46 expression within the hCD45+ cells. B cells were marked by CD19 and CD20 expression within human CD45+ cells. Surface IgG or IgM positive cells were selected by IgM and IgG positive cells within B cells. Plasmacytoid dendritic cells were selected by exclusion of CD16+, CD14+, CD11B+ cells within human immune cells and had low or no expression of CD11c. All frequencies are either reported out of hCD45+ cell populations or their parent gate. Mouse immune cells were reported based on mouse CD45 expression excluding human CD45 cells. Mouse neutrophils were reported based Ly6G expression and SSC high profile of mouse immune cells. Cell numbers were calculated by using counting beads (Biolegend).

☒ Tick this box to confirm that a figure exemplifying the gating strategy is provided in the Supplementary Information.